



Computational metallurgy and changes of scale / Métallurgie numérique et changements d'échelle Multiscale modeling of ductile failure in metallic alloys

Modélisation multi-échelle de la rupture ductile des alliages métalliques

Thomas Pardoen^{a,*}, Florence Scheyvaerts^a, Aude Simar^a, Cihan Tekoğlu^a, Patrick R. Onck^b

^a Institute of Mechanics, Materials and Civil Engineering, Université catholique de Louvain, place Sainte Barbe 2, B-1348 Louvain-la-Neuve, Belgium

^b Micromechanics of Materials, Zernike Institute for Advanced Materials, University of Groningen, Nijenborgh 4, NL-9747 AG Groningen, The Netherlands

ARTICLE INFO

Article history:

Available online 25 August 2010

Keywords:

Ductile fracture
Multiscale modelling
Ductility
Fracture toughness
Damage
Voids

Mots-clés :

Rupture ductile
Modélisation multi-échelle
Ductilité
Ténacité
Endommagement
Cavités

ABSTRACT

Micromechanical models for ductile failure have been developed in the 1970s and 1980s essentially to address cracking in structural applications and complement the fracture mechanics approach. Later, this approach has become attractive for physical metallurgists interested by the prediction of failure during forming operations and as a guide for the design of more ductile and/or high-toughness microstructures. Nowadays, a realistic treatment of damage evolution in complex metallic microstructures is becoming feasible when sufficiently sophisticated constitutive laws are used within the context of a multilevel modelling strategy. The current understanding and the state of the art models for the nucleation, growth and coalescence of voids are reviewed with a focus on the underlying physics. Considerations are made about the introduction of the different length scales associated with the microstructure and damage process. Two applications of the methodology are then described to illustrate the potential of the current models. The first application concerns the competition between intergranular and transgranular ductile fracture in aluminum alloys involving soft precipitate free zones along the grain boundaries. The second application concerns the modeling of ductile failure in friction stir welded joints, a problem which also involves soft and hard zones, albeit at a larger scale.

© 2010 Académie des sciences. Published by Elsevier Masson SAS. All rights reserved.

RÉSUMÉ

Les modèles micromécaniques pour la rupture ductile ont été développés essentiellement au cours des années 1970 et 1980 avec comme but de traiter des problèmes de rupture dans des applications structurales et de compléter l'approche par la mécanique de la rupture. Plus tard, cette approche micromécanique a attiré les spécialistes de la métallurgie physique soucieux de prédire les problèmes de rupture pendant les opérations de mise en forme ainsi que d'être guidés pour l'élaboration de microstructures plus ductiles et/ou plus tenaces. Aujourd'hui, il est devenu possible d'aborder de façon réaliste l'évolution du dommage dans des microstructures métalliques complexes à condition d'utiliser des lois constitutives suffisamment sophistiquées dans le contexte d'une stratégie de modélisation multi-échelle. La compréhension actuelle et l'état de l'art dans la modélisation des phénomènes de germination, croissance et coalescence de cavités sont passés en revue en portant une attention particulière à la physique sous-jacente. La prise en compte des différentes longueurs caractéristiques associées à la microstructure et au processus d'endommagement est discutée. Deux applications de la méthodologie sont décrites pour illustrer le potentiel des modèles. La première application concerne la compétition entre

* Corresponding author.

E-mail address: thomas.pardoen@uclouvain.be (T. Pardoen).

rupture ductile intergranulaire et transgranulaire dans des alliages d'aluminium impliquant des zones molles sans précipité le long des joints de grain. La seconde application concerne la modélisation de la rupture ductile de joints soudés par friction malaxage, un problème qui implique également des zones dures et molles, mais à une échelle plus grande.

© 2010 Académie des sciences. Published by Elsevier Masson SAS. All rights reserved.

1. Introduction

Ductile failure of metals is a broad topic connected to several engineering issues from the assessment of failure in primary structural components, the damage evolution during high and low temperature forming applications, to the optimization of complex metallic alloys for improved crashworthiness. Structural integrity assessment, especially within the nuclear industry, has been the first motor for the development of a micromechanical approach of ductile failure, also called “local approach of ductile fracture” in the French terminology, in the 1970s and 1980s, see reviews in [1–4], following seminal studies by Tipper [5], Puttick [6], Rogers [7], Beachem [8], Gurland and Plateau [9], McClintock [10], and Rice and Tracey [11]. The interest for micromechanical models was mainly driven by the fracture mechanics community to simulate crack growth in ductile materials and solve the problem of transferability of results generated from laboratory specimens to structural components when a safe use of the fracture mechanics concepts cannot be insured, see e.g. [12–16]. Applications to other key structural problems followed, involving, for instance, cracking in pipelines, in airplane structures, or in high pressure tanks. All these applications were essentially motivated by problems involving pre-existing cracks and by the need to predict the risk of unstable crack propagation. At the tip of a crack, the stress triaxiality – defined as the ratio of the hydrostatic stress over the effective stress – is high and voids grow relatively fast without significant shape change, e.g. [14,17]. The constitutive models used in the 1980s were good enough to treat this class of problems.

In the 1990s and later, researchers were interested in applying these models to physical metallurgy problems, such as those encountered in forming applications [18–21] or in the design of metallic alloys involving complex microstructures and competition of failure modes [22–25]. Indeed, primary forming applications such as extrusion, rolling or wire drawing are sometimes limited by damage accumulation. In that case, low stress triaxiality conditions prevail and issues related for instance to void shape evolution became important [20,26]. New developments were thus needed to improve the models in order to encompass both low and high stress triaxiality regimes, a problem which is also essential when addressing thin sheet ductile tearing [27,28]. Regarding microstructure design, although the attention has been systematically focused for decades in metallurgy towards enhancing the strength, the controlled generation of ductile, high fracture toughness microstructures is still a field of open improvement. For instance, new alloys such as the multiphase TRIP steels [29] or new bimodal Ti alloys [30] sometimes suffer from a lack of cracking resistance, limiting their application. In essence, ductile failure in these materials is multiscale, starting at the size of the voids and involving interaction with various microstructural features.

The goal of this article is to introduce recent progress in the field of multiscale modelling of ductile failure with a viewpoint on its application in physical metallurgy in order to guide the development of new metallic alloys. The focus is on ductile failure through the accumulation of damage, not through plastic localization which is another important issue in some forming applications. The physical mechanisms of ductile failure are briefly reviewed in Section 2. Section 3 presents a selected and partial survey of the multiscale modeling of ductile failure, representative of the state of the art in the field. Two applications involving several different length scales are given in the last two sections for the sake of illustration. Finally, Section 6 concludes this paper.

2. Survey of ductile failure mechanisms

The following description of the micromechanisms of ductile failure is based both on experimental observations and on numerical experiments performed using finite element unit cell calculations.¹ The generic phenomenology is described in Fig. 1. A macroscopic specimen, here with a notch, is deformed in tension. Damage develops faster in the centre of the minimum cross-section of the bar which involves the highest stress triaxiality as well as large plastic strains, the two main parameters in ductile fracture [1,4,11].

The failure process starts by the nucleation of voids on second phase particles, either through the fracture of the particles or by partial or full decohesion of the interface between the particle and the surrounding matrix [31]. Void nucleation tends to occur first on large particles due to a larger probability of defects, as well as within particle clusters where large stress levels are attained in the particles [32]. Metallic alloys sometimes involve several populations of particles, nucleating voids

¹ Void cell simulations consist of modelling one or a limited number of voids, surrounded by a matrix material, using the FE method, by assuming a simple distribution, often periodic. The cell is deformed up to large strains and the applied stress, as well as other quantities of interest, such as the void volume fraction and shape, are extracted from the calculations. It is a good alternative to difficult experiments to investigate the response of an ideal, voided material volume element. In addition, void cell simulations offer a basis for assessing the validity of constitutive models, before applying them to more complex and more realistic problems.

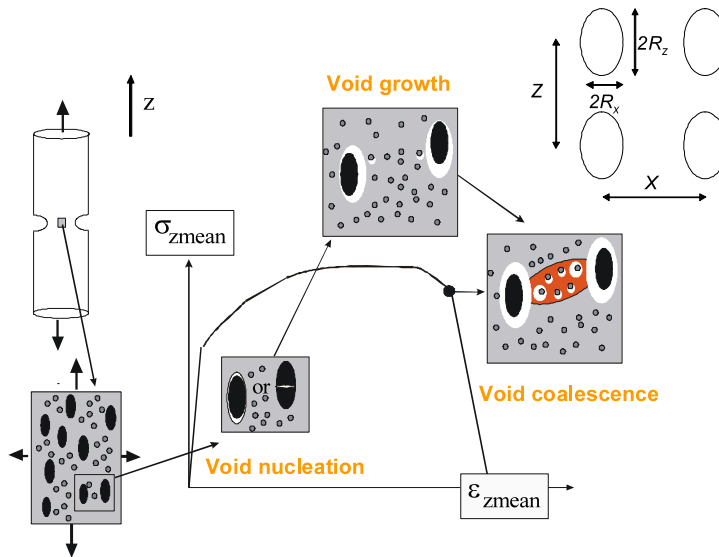


Fig. 1. Schematic description of the sequence of damage mechanisms leading to ductile failure in metallic alloys.

Fig. 1. Description schématique de la séquence des mécanismes d'endommagement conduisant à la rupture ductile d'alliages métalliques.

at different levels of loading. These populations can distribute in various ways, with, for instance, one population located along the grain boundaries, and another population homogeneously dispersed inside the grains, or with two very different sizes. The maximum volume fraction of voids nucleating in industrial metals is lower than 2–3% and often much smaller, lower than 0.01% in clean alloys.

Once nucleated, the voids grow by plastic deformation, with the plastic flow distributed all around the voids. Initially rounded voids dilate and elongate at low stress triaxiality and dilate much more at high stress triaxiality for the same level of deformation with much less shape changes [26,33]. Initially flat voids, nucleated as a result of a particle fracture or by partial interface failure, grow primarily by opening in the direction normal to the small void dimension [34,35]. Plastic anisotropy also affects the void growth rate and shape evolution [36–39]. Increasing the strain hardening and/or the strain rate sensitivity tends to moderately decrease the void growth rate [19,35]. As voids nucleate over a range of strain, the nucleation and growth stages co-exist, leading to voids with different shape and sizes. Interactions between voids are weak when the neighboring voids have similar sizes, i.e. a void is not growing significantly faster in the presence of a close neighbor [40]. This justifies the assumption, for modelling ductile failure, of using only an average void volume fraction and average void aspect ratio during the void growth stage, without accounting for void distribution effects. The picture can become more complex in multiphase materials or systems involving for instance two different types of void nucleation mechanisms leading to very different initial void shapes. Also, when a very small void is located in the close neighborhood of a much larger void, the growth rate of the small void is significantly accelerated due to the strain concentration developing around the large void [41].

Before the voids link up, a change in the plastic flow mechanism takes place with the plastic deformation suddenly localizing in the ligament between the most closely spaced voids [3,42]. This localization is called the onset of void coalescence which interrupts the mechanism of relatively homogeneous void growth and constitutes the beginning of the final stage of damage. In the most ductile metals, the void size doubles or even triples before coalescence sets in. In less ductile metals, coalescence starts immediately after nucleation, involving almost no void growth. The mechanism is then said “nucleation controlled” [43,44]. The coalescence of voids consists thus of a transition from a stable phase of diffuse plastic deformation driving the stable growth of the voids to a localized mode of plastic deformation within the ligament separating two voids or a row of voids, with material off the localization plane undergoing elastic unloading. The first mode of coalescence is the *internal necking* mode of coalescence, where the ligament between the two voids shrinks with a shape typical of a necking process. During the process of coalescence, the voids evolve towards a diamond shape. The second mode of void coalescence consists in a *shear localization* between the voids observed when the initial voids are distributed along lines at 45° from the main loading direction. This mode of coalescence is frequently observed in high strength material with low or moderate strain hardening capacity. The third mode of void coalescence, called “*necklace coalescence*” [38] is less common. It consists of a localization process in a direction parallel to the main loading axis and has been observed to take place in rows of closely spaced voids gathering within aligned clusters of particles.

One must distinguish the onset of void coalescence and the coalescence phase. The end of the coalescence process usually consists, for the most ductile metals, in the radial void growth up to final impingement. In less ductile metals, coalescence is interrupted due to a premature failure of the remaining ligament by microcleavage, crystallographic shearing, or with the help of a second population of smaller voids [45–48]. Void distribution effects, especially the relative void spacing between

the closest neighbors, play a dominant role in controlling the onset of void coalescence [42,49,50], while, as explained above, it has a negligible effect during the void growth stage. Cracking initiation can be defined as when a couple of voids have coalesced locally in the most loaded region of a specimen or of a structural component. The local deformation corresponding to cracking initiation is the physical measure of the material ductility. Under low stress triaxiality, the extra overall deformation required to bring a material element from the onset of coalescence to final coalescence is negligible compared to the total strain. The ductility or fracture strain can then be approximated as the strain corresponding to the onset of void coalescence. However, under high stress triaxiality conditions, an important part of the total energy associated to the damage process is spent during coalescence and an accurate prediction of the end of the fracture process is important [51]. The void growth rate being proportional to the exponential of the stress triaxiality [11], the fracture strain decreases with increasing stress triaxiality [19,21,34,52,53].

Cracking initiation does not signify the complete failure of a sample or of a structural component; the failure process ends by the propagation of the crack requiring additional deformation whose magnitude depends on the geometry and loading configuration. In a classical tensile test where failure occurs within the necking region, this additional strain corresponding to the ductile tearing process is relatively small, e.g. [54]. Furthermore, the strain being relatively homogeneous in the neck, the strain estimated from the measurement of the minimum cross-section of the broken specimen is a good approximation of the local strain at cracking initiation, which is the true measure of the ductility. The same approximation can sometimes be made for cylindrically notched specimens with shallow notches.

Crack propagation occurs by repeated coalescence of voids at the crack tip within the so-called fracture process zone. At sufficiently high porosity, the void near the crack tip is influenced by its nearest neighbor, which experiences almost the same rate of growth [55]. The interaction among the voids, including voids even farther from the tip, results in significantly higher rate of void growth for all of the voids. Coalescence among several voids and with the crack starts early, almost simultaneously. This is the *multiple void interaction* mechanism. For sufficiently small void volume fraction, a single void process prevails. The void nearest the tip grows with little influence from its nearest neighbor further from the tip. This is the so-called *void by void growth* mechanism [55]. Depending on the geometry, loading configuration and material strength, the crack can run straight or following a zig-zag path, or it can kink along a maximum shear direction such as for the cup and cone fracture in tensile testing [56,57]. Whether the crack results from a void coalescence process or pre-exists such as in a fracture mechanics specimen, a length scale enters the ductile failure process during crack propagation. Indeed, damage localizes within a band of thickness scaling with the void spacing X_0 .

Based on this general picture of the ductile failure process and the regularities observed in the mechanisms of nucleation, growth and coalescence, the problem can be significantly simplified by treating the behavior of a representative volume element containing one void extracted from a periodic distribution. Simple damage evolution laws or, better, full constitutive models have been developed to capture these elementary mechanisms, as described in the next section. The damage in one elementary cell can be characterized by the following parameters, see the insert in Fig. 1:

- f , the void volume fraction, with initial value f_0 directly connected to the particle volume fraction f_p ;
- $W = R_z/R_x$, the void aspect ratio, assuming spheroidal void shape with main radius R_z and R_x , and W_0 , the initial value being very small in the case of particle fracture or equal to the particle aspect ratio for complete interface decohesion;
- $\chi = 2R_x/X$, the relative void spacing in the x direction (which is perpendicular to the main loading direction) assumed to be aligned with ligament in which coalescence sets in, with χ_0 the initial value;
- $\lambda = Z/X$, the void distribution parameter with X and Z being the mean spacing in the x and z direction respectively, and λ_0 the initial value.

These parameters are related through the following expression:

$$\chi = \left(\frac{f \lambda}{\zeta W} \right)^{\frac{1}{3}} \quad (1)$$

where ζ is a geometric factor which depends on the void distribution: $\zeta = \pi/6 = 0.523$ for a periodic simple cubic array, $\zeta = \sqrt{3}\pi/9 = 0.605$ for a periodic hexagonal distribution and $\zeta = 2/3 = 0.666$ for a void surrounded by a cylindrical matrix.

In the case of this simplified representation of the microstructure, the ductility/fracture strain of metallic alloys can be written in general terms:

$$\varepsilon_f = F \left(T, \frac{\sigma_n}{\sigma_0}, n, f_0, W_0, \lambda_0, \text{other microstructural features} \right) \quad (2)$$

where T is the stress triaxiality, σ_n is an average critical stress for particle fracture or decohesion, σ_0 is the initial yield stress, and n is a strain hardening index. Regarding the fracture toughness, dimensional analysis shows that, see [55,58] for more details:

$$\frac{J_{Ic}}{\sigma_0 X_0} = F \left(\frac{\sigma_0}{E}, n, f_0, W_0, \lambda_0, \frac{\sigma_n}{\sigma_0}, \text{other microstructural features} \right) \quad (3)$$

where E is the Young's modulus. The length X_0 directly enters the fracture toughness defined as the value of the energy release rate or of the J -integral at cracking initiation starting from a pre-existing sharp crack, J_{Ic} , in mode I. As discussed

later in Section 3.3 and in the examples of Sections 4 and 5, other lengths than X_0 play a role in ductile failure and affect the total energy dissipated during the deformation and damage process.

The idea that a generic sequence of elementary damage mechanisms occurs in most ductile metallic systems simplifies the multilevel modelling of failure by allowing a generic treatment of the lowest scale response. This motivates to present first the state of the art modelling of the elementary damage mechanisms in the next section.

3. Multiscale modeling of ductile failure in metals

3.1. Void nucleation and void growth models

In recent years, the modeling of void growth in metals has attained a high level of sophistication. In contrast, progress regarding the development of closed form void nucleation models – that can be incorporated into the existing damage evolution schemes – has been much more limited.

In either case of particle fracture or particle–matrix interface decohesion, an accurate description of void nucleation necessitates an accurate estimate of the stress/strain values at and round the particles. Recently, Tekoğlu and Pardoen [44] proposed to make a step further in the description of void nucleation by integrating a damage model with a Mori–Tanaka type mean-field homogenization scheme, which explicitly accounts for the per-phase behavior. The benefit of this integrated Mori–Tanaka damage (IMTD) model is two-fold: (i) it provides a physically sound prediction of the void nucleation rate and its dependence on the stress state, through an accurate prediction of the load transfer between the particle and the matrix; (ii) it accounts for the increase of the overall strength and strain hardening of the material due to the presence of the particles, as well as for the softening associated with the decrease in the load carrying capacity of the particles due to void nucleation. The IMTD model provides an advanced framework to discuss ductile failure in multiphase alloys; its presentation allows having a close look at state of the art ductile fracture models while also recalling earlier fundamental works.

As discussed in Section 2, ductile fracture is composed of consecutive and overlapping phenomena of nucleation, growth, and coalescence of voids. Both the growth and nucleation of voids contribute to the total rate of increase of porosity, which can be written as

$$\dot{f} = \dot{f}_{growth} + \dot{f}_{nuc} \quad (4)$$

Considering the plastic incompressibility of the surrounding matrix, the rate of increase of porosity due to void growth reads

$$\dot{f}_{growth} = (1 - f)\dot{\epsilon}_{ii}^p \quad (5)$$

where $\dot{\epsilon}_{ii}^p$ is the trace of the plastic strain rate tensor.

The Gurson model [59] has been the first widely used micromechanical model for ductile rupture which introduces a strong coupling between deformation and damage. It is based on a simplified representation of a voided material which consists in a hollow sphere. The only non-dimensional microstructural feature in the model is the void volume fraction or porosity, f . The matrix obeys a standard von Mises yield criterion and associated flow rule. The main result of the upper bound analysis of Gurson is an estimate of the yield function for the porous metal which, applying the normality rule, can be used to derive the plastic flow direction. Gologanu et al. [26,60,61] reworked the Gurson model in order to account for spheroidal void shapes (for an overview of the recent improvements of the Gologanu–Leblond–Devaux (GLD) void growth model, see e.g. [4,62]). For simplicity, here we will deal only with axisymmetric loading conditions where the main void axis, say \mathbf{e}_z , does not rotate and remains parallel to the maximum principal stress. In this case, the GLD model gives the evolution of the void aspect ratio as

$$\frac{\dot{W}}{W} = (1 + h_S h_T h_f)(\dot{\epsilon}_{zz}^p - \dot{\epsilon}_{xx}^p) + h_{Sf} \dot{\epsilon}_{ii}^p \quad (6)$$

where the h parameters are functions of the void aspect ratio W , porosity f , stress triaxiality T , and a power law strain hardening exponent n , see also Pardoen and Hutchinson [63]. The plastic strain rate $\dot{\epsilon}_{ij}^p$ is normal to the flow potential ϕ :

$$\dot{\epsilon}_{ij}^p = \dot{\gamma} \frac{\partial \phi}{\partial \sigma_{ij}} \quad (7)$$

with

$$\phi = \frac{C}{\sigma_y^2} (\sigma_{zz} - \sigma_{xx} - \eta \sigma_h)^2 + 2q(g+1)(g+f) \cosh\left(\kappa \frac{\sigma_h}{\sigma_y}\right) - (g+1)^2 - q^2(g+f)^2 = 0 \quad (8)$$

where σ_{ij} are the components of the Cauchy stress tensor and σ_h is the hydrostatic stress. In Eq. (8), the parameters C , η , g and κ are functions of W and f , and q is an adjusting parameter (see also [20,63]). The energy balance proposed by Gurson [59]

$$\sigma_y \dot{\epsilon}^p (1 - f) = \sigma_{ij} \dot{\epsilon}_{ij}^p \quad (9)$$

where σ_y is the current average yield stress of the material, is used to calculate the effective plastic strain rate $\dot{\underline{\underline{\epsilon}}}^p$. Up to this point, the formulation of the IMTD model is the same as previous ductile damage models based on the GLD constitutive behavior. In earlier models, σ_y refers to the average yield stress of the surrounding single-phase matrix material, and is given by a simple hardening law. In the IMTD model, however, σ_y represents the average yield stress of the surrounding multi-phase matrix material (i.e. a metal alloy or a composite material), and is calculated through a non-linear Mori–Tanaka homogenization scheme which explicitly accounts for the presence of second phase particles. The non-linear, rate independent Mori–Tanaka (MT) scheme gives the macroscopic response of the composite as

$$\langle \dot{\underline{\underline{\sigma}}} \rangle = \underline{\underline{\underline{C}}} : \langle \dot{\underline{\underline{\epsilon}}} \rangle \quad (10)$$

$$\underline{\underline{\underline{C}}} = [v^i \underline{\underline{\underline{C}}}^i : \underline{\underline{\underline{A}}}^i + (1 - v^i) \underline{\underline{\underline{C}}}^M] : [v^i \underline{\underline{\underline{A}}}^i + (1 - v^i) \underline{\underline{\underline{I}}}]^{-1} \quad (11)$$

$$\underline{\underline{\underline{A}}}^i = [\underline{\underline{\underline{I}}} + \xi : (\underline{\underline{\underline{C}}}^M)^{-1} : \underline{\underline{\underline{C}}}^i - \underline{\underline{\underline{I}}}]^{-1} \quad (12)$$

where single and double underbars represent second and fourth order tensors, and the superscripts “M” and “i” stand for matrix and particle, respectively, $\underline{\underline{\underline{I}}}$ is the fourth order identity tensor, v^i is the volume fraction of the particles, $\underline{\underline{\underline{C}}}$ is the macroscopic tangent operator of the composite, ξ is the Eshelby tensor, and $\underline{\underline{\underline{A}}}^i$ is the strain concentration tensor which relates the average strain rate in the particle $\langle \dot{\underline{\underline{\epsilon}}}^i \rangle$ to that in the matrix $\langle \dot{\underline{\underline{\epsilon}}}^M \rangle$ through

$$\langle \dot{\underline{\underline{\epsilon}}}^i \rangle = \underline{\underline{\underline{A}}}^i : \langle \dot{\underline{\underline{\epsilon}}}^M \rangle \quad (13)$$

The Eshelby tensor ξ depends on the particle geometry and the tangent operator of the matrix, $\underline{\underline{\underline{C}}}^M$. Numerical simulations show that using $\underline{\underline{\underline{C}}}^M$, which is an anisotropic tensor even for an isotropic matrix, to calculate the Eshelby tensor leads to very stiff predictions, while using only an isotropic part of the tangent operator of the matrix, $\underline{\underline{\underline{C}}}^{M_{iso}}$, provides much better predictions in terms of the overall response of the composite (e.g. see the work by Doghri and coworkers [64–66]). $\underline{\underline{\underline{C}}}^{M_{iso}}$ can be defined as

$$\underline{\underline{\underline{C}}}^{M_{iso}} = (\underline{\underline{\underline{I}}}^{vol} :: \underline{\underline{\underline{C}}}^M) \underline{\underline{\underline{I}}}^{vol} + \frac{1}{5} (\underline{\underline{\underline{I}}}^{dev} :: \underline{\underline{\underline{C}}}^M) \underline{\underline{\underline{I}}}^{dev} \quad (14)$$

where $\underline{\underline{\underline{I}}}^{vol}$ and $\underline{\underline{\underline{I}}}^{dev}$ are respectively the spherical and deviatoric parts of the identity tensor (Bornert et al. [67]). In the IMTD model, a two-step recursive homogenization scheme is used which employs both $\underline{\underline{\underline{C}}}^M$ and $\underline{\underline{\underline{C}}}^{M_{iso}}$. The idea is to divide the composite into two subsystems, s1 and s2, with volume fractions v^{s1} and v^{s2} ($= 1 - v^{s1}$), and calculate the Eshelby tensor ξ using $\underline{\underline{\underline{C}}}^M$ for s1 and $\underline{\underline{\underline{C}}}^{M_{iso}}$ for s2, see Tekoğlu and Pardoën [44] for details about the estimation of v^{s1} .

Previous models in the literature involved simple void nucleation laws that are based on either overall stress and/or strain values (e.g. Chu and Needleman [68]), or an approximate analytical estimate of the stress in the particle (Beremin [69]); as a result, these models do not have any coupling either with the hardening of the material due to the presence of the second phase particles, or with the softening due to void nucleation (i.e. particle fracture or particle–matrix interface decohesion). In the IMTD model, void nucleation is directly related to the stress in the particle or along the particle–matrix interface, calculated by the MT homogenization scheme described above. The schematic diagram in Fig. 2 shows the flow chart for the IMTD model. At each strain increment, the MT scheme calculates the overall as well as the per-phase response of the composite, and transfers the elastic and plastic moduli of the composite to the GLD model, and the maximum principal stress in the particle to the void nucleation box. By this way, the GLD porous plasticity interacts with the composite surrounding the voids as if it was a homogeneous matrix. Assuming that there are no pre-existing voids, the response of the composite is entirely predicted by the MT scheme before void nucleation. When the maximum principal stress in a particle, σ_{princ}^{p-max} , reaches a critical value, σ_c^{min} , void nucleation starts. The value of σ_c^{min} is different for particle fracture than for particle–matrix interface decohesion. The increase in porosity due to void nucleation can be given as

$$\Delta f_{nuc} = \frac{W_0}{W_p} \Delta v^p \quad (15)$$

where W_0 is the initial void aspect ratio (i.e. immediately after nucleation), W_p the particle aspect ratio, and Δv^p the volume fraction of the particles that nucleated voids. After giving birth to voids, particles lose part of their load carrying capacity. The decrease in the load carrying capacity of particles is taken into account in the IMTD model by decreasing a corresponding amount of particle volume fraction in the MT homogenization scheme, which is expressed as $\Delta v_{nuc}^p = \delta \Delta v^p$, with δ being a heuristic parameter, see Tekoğlu and Pardoën [44] for details. In order to take the stochastic nature of the void nucleation phenomenon into account, the IMTD model assumes that void nucleation, which starts at $\sigma_{princ}^{p-max} = \sigma_c^{min}$, continues through a range of particle stress, $\Delta \sigma_c$, within which each value corresponds to a different particle size and shape. After the onset of void nucleation, the void nucleation box transfers the associated increase in porosity, Δf_{nuc} , to the GLD model, where void growth and void shape changes are calculated. With further plastic deformation voids get closer to each other and coalescence starts, based on a criterion such as the one discussed in Section 3.2.

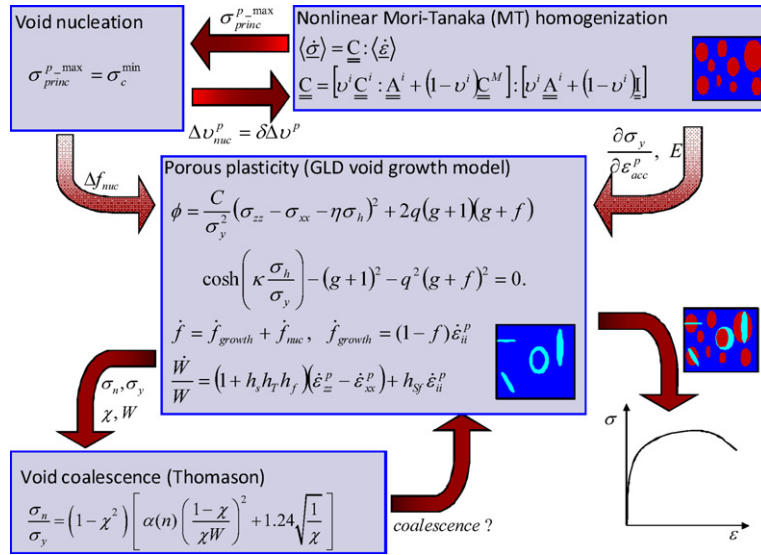


Fig. 2. Schematic diagram showing the flow chart for the integrated Mori-Tanaka damage (IMTD) model.

Fig. 2. Diagramme schématique de l'algorithme du modèle intégré d'endommagement et d'homogénéisation par l'approche de Mori-Tanaka (IMTD).

Even though relatively sophisticated in terms of mathematical developments, the IMTD model is conceptually rather simple, and it recognizes the intimate coupling between the strain hardening of the composite and the presence of the second phase particles, as well as the softening of the composite and the nucleation and growth of voids. The parameters that need to be identified to use in the IMTD model, and which are typical of many other versions of the Gurson model, are λ , which measures the anisotropy in particle (therefore void) distribution, σ_c^{\min} , the critical particle stress value at which void nucleation starts, $\Delta \sigma_c$, the range of particle stress through which void nucleation continues, and v^{s1} , the volume fraction of subsystem-1 in the MT scheme, see above. Except for v^{s1} , all these parameters have a clear physical meaning; although they cannot be directly measured experimentally, they can be decided by inverse identification.

The current state of the art modeling of void growth relies on extensions of the Gurson model, such as the standard Gologanu and the IMTD models. Many other contributions have flourished over recent years involving extensions to strain hardening, e.g. [39,63,70], to strain rate sensitive materials [19,71] to plastic anisotropy [37–39,62,72–74], to kinematic hardening [75–77], and to shear loadings [78].

3.2. Void coalescence models

Significant progress has been made over the last 5–10 years in the modeling of void coalescence, moving from very simple empirical critical porosity or critical strain based coalescence models to more advanced micromechanics based models. This is indeed an important building block of any predictive microstructure-informed ductile damage model. The starting point for most of the recent progresses is the void coalescence condition proposed by Thomason based on a slip line solution [42,79,80] which writes (in its most elaborate form)

$$\frac{\sigma_n(\delta)}{\sigma_y^{loc}(1-f_2)} = (1-\eta\chi^2(\delta)) \left[\alpha \left(\frac{1-\chi(\delta)}{\chi(\delta)W(\delta)} \right)^2 + \beta \sqrt{\frac{1}{\chi(\delta)}} \right], \quad \text{for } \delta \in [0; \pi/2] \quad (16)$$

where σ_n is the overall stress component normal to the localization band oriented in the direction δ , σ_y^{loc} is a representative yield stress equal to σ_0 in the original version (the model was initially developed for perfectly plastic materials), f_2 is the volume fraction of secondary voids ($f_2 = 0$ in the original model), α and β are constants, equal to 0.1 and 1.24, respectively, and η is a geometric factor which depends on the void arrangement (η is defined such that the term $1/(1-\eta\chi^2)$ represents the ratio of the total ligament area including the void divided by the non-porous area; in a cylindrical void cell $\eta = 1$). Thomason's criterion (16) is a condition for the onset of coalescence in the ligament between neighboring voids by internal necking. It states that coalescence occurs when the stress normal to the localization plane σ_n/σ_y reaches a critical value. This critical value decreases as the voids open (W increases) and get closer to each other (χ increases). The dominant parameter controlling the transition to the coalescence mode is the relative void spacing χ . When combined to a void nucleation/void growth model such as the one presented in Section 3.1 to estimate σ_n , χ , calculated using Eq. (1), and W , the transition into coalescence is predicted to occur when Eq. (16) is fulfilled, meaning that the solution for a localized plastic flow starts prevailing over the solution for a more diffuse mode of plasticity around the voids. The use of the Thomason criterion (16) thus heavily relies on an accurate prediction of the evolution of the flow and damage variables

before coalescence. Three recently proposed extensions of Thomason's coalescence criterion developed to generalize and enhance its predictive potential are briefly described hereafter.

3.2.1. The first generalization

The first generalization consists of properly accounting for the orientation of the void localization plane. Indeed, the void axes are not necessarily aligned with the principal loading directions and the ligament where coalescence takes place is not necessarily transverse to the maximum principal stress. The details of the extension are given in [81]. The main ideas are the following. The centers of the voids are assumed to be initially statistically homogeneously distributed in the deformation plane following an ellipsoidal symmetry [82]. Material compatibility requires that the void center distribution follows the material deformation and evolves such as to remain elliptical. An effective void aspect ratio $W(\delta)$ and an effective relative void spacing $\chi(\delta)$ are heuristically defined as a function of the orientation of the localization plane δ . The criterion is checked for every angle δ while σ_n is taken as the stress normal to the ligament. After condition (16) has been met for one orientation $\delta = \delta_c$, plastic localization takes place in the ligament separating the two neighboring cavities. This extension is essential when dealing with elongated voids not necessarily aligned with the main loading direction or in the case of shear deformations. To a good approximation and except for a few relatively exotic cases, the localization plane is exactly or almost normal to the maximum principal stress direction, which could simplify the implementation of the model.

3.2.2. The second generalization

The second generalization concerns strain hardening. In order to account for the effect of the strain hardening in condition (16), a dependence of the parameter α on the strain hardening exponent n has been proposed by Pardoen and Hutchinson [63] based on a large number of axisymmetric FE cell calculation results: $\alpha = 0.1 + 0.217n + 4.83n^2$ (with n defined within a power law hardening fit and varying between 0 and 0.3). In addition, σ_0 is replaced by the current mean yield stress σ_y of the matrix material estimated using the energy balance (9). Another more elegant way to introduce strain hardening in the Thomason's criterion is based on the idea that the localization process is triggered by the weakest point along the ligament line which anticipated to be the most deformed spot. The localization should thus be controlled by the local value of the current yield stress σ_y^{loc} instead of the current average yield stress σ_y resulting from Eq. (9). The local yield stress is related to the local accumulated plastic strain ε_y^{ploc} through the hardening law. FE cell calculations have shown that the largest accumulated plastic strain is always found near the surface of the void in the intervoid ligament. The local strain rate components in the region next to the surface of a void, $\dot{\varepsilon}_{ij}^{ploc}$ can be related to the applied strain rates and to the rate of change of the void dimensions based on simple geometrical arguments, described in [48,81,83]. This new version of the Thomason model has been successfully validated based on a large set of 3D FE void cell simulations performed for different material parameters, loading conditions, and strain hardening laws, for both J2 elastoplasticity [81] and single crystal plasticity description of the matrix [83].

3.2.3. The third extension of the void coalescence criterion (16)

The third extension of the void coalescence criterion (16) aims at introducing the effect of a second population of voids. As mentioned in Section 2, the damage process controlled by the growth and coalescence of primary voids nucleated on particles with a size varying typically between 1 and 100 μm is sometimes affected by the growth of much smaller secondary voids nucleated on inclusions with a size varying typically between 0.1 and 3 μm , see Fig. 1. The nucleation and growth of secondary voids do essentially not affect the growth of the primary voids but mainly accelerate the void coalescence process by softening the material in the ligament between the voids where the strains are very large. The softening induced by the growth of secondary voids is introduced by multiplying the yield stress of the matrix material by $(1 - f_2)$, with f_2 being the maximum value of the secondary voids volume fraction over the ligament. This maximum is always attained next to the surface of the primary voids where the plastic strains are the largest. This extension and its validation has been guided by FE void cell calculations in which the second population is introduced by using the Gurson model to represent the behavior of the matrix surrounding the primary void [48], following earlier works by Brocks et al. [84] and Gao and Kim [85]. This model assumes that the secondary voids are much smaller than the primary voids. The drop of the ductility caused by the presence of secondary voids increases if the nucleation strain decreases and/or if their volume fraction increases, and these effects are properly captured by the new extension of the Thomason criterion.

3.2.4. Model for the coalescence stage

Finally, a model for the coalescence stage must be provided in order to represent the final drop of the load carrying capacity. After condition (16) has been met for one orientation $\delta = \delta_c$, plastic localization takes place in the ligament separating the two cavities with the strain rate parallel to the ligament becoming very small, leading to a state of uniaxial straining (see e.g. Koplik and Needleman [86]). The only non-zero plastic strain component develops along the normal to the ligament. A simple geometric model has been worked out for deriving the unloading slope, required to bring a material element from the onset of void coalescence up to final fracture. This slope controls the amount of energy dissipated during coalescence. The details of the derivation are provided in Scheyvaerts et al. [51], resembling the analysis by Benzerga [87]. The normal stress to the ligament σ_n is assumed to decrease linearly with the normal strain ε_n . This linear evolution has been verified by Tvergaard [88] up to very large strains using a remeshing procedure. The strain increment $\Delta\varepsilon_n$ needed to bring a material element from the onset of coalescence to full failure is estimated by making several geometric assumptions:

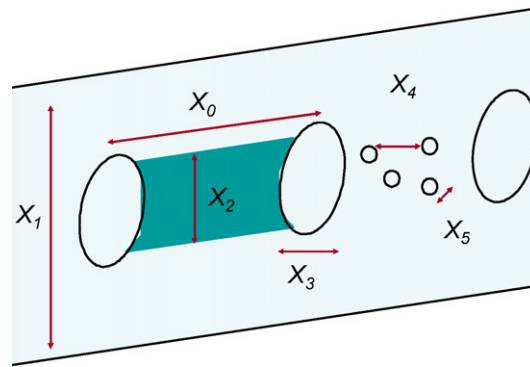


Fig. 3. Schematic description of the lengths entering a generic ductile damage process.

Fig. 3. Description schématique des échelles caractéristiques qui peuvent être impliquées dans un processus d'endommagement ductile.

(i) uniaxial straining is enforced during coalescence; (ii) the localization zone shape is approximated by a straight band; (iii) the voids evolve towards a diamond shape; (iv) fracture occurs by void impingement, neglecting possible accelerating factors such as the presence of a second population of voids or microcleavages taking place within the ligament; elastic strains are neglected; (v) a scaling between the height of the localization band and the ligament length following the mechanics of necking. The model has been assessed by comparison to a large set of FE cell calculations. In most instances, the error on $\Delta\varepsilon_n$ is lower than 20%.

Other recent extensions/improvements in the modeling of void coalescence involve accounting for the effect of shear [89] or of the rate sensitivity [71].

3.3. Scale transition and size issues

Several physical lengths play a role in ductile fracture as schematically represented in Fig. 3. The primary parameter controlling the onset of void coalescence, hence the ductility, is the relative spacing between voids. The relative void spacing is set by the microstructure and is directly related to the ratio of the particle size to the particle spacing. It depends thus on the distribution of particles as well as on the statistical distribution of void nucleation events. Now, χ is only a relative dimension and the ductility seems thus, in the context of the models described above, not being affected by any absolute length scale. There are many instances, however where this conclusion is not correct and true size effects enter the problem.

The particle size can have both a direct and an indirect effect on the ductility. It has been shown theoretically that voids with a diameter X_3 , see Fig. 3, typically smaller than $1\ \mu\text{m}$ grow more slowly than larger voids due to strain gradient plasticity effects [90]: the accumulation of a high density of geometrically necessary dislocations around such small voids tends to decrease the void growth rate. The effect of the initial void size has been accounted for by reworking the Gurson model in the case of the Taylor dislocation based strain gradient plasticity model, e.g. [91]. However, direct experimental evidence of slower void growth rates is still lacking. An indirect effect of changing the particle size is related to the modification of the void nucleation condition. Decreasing the particle size down to the micrometer range or smaller induces strain gradient plasticity effects, affecting the load transfer to the particle [92]. Furthermore, smaller particles statistically contain fewer defects than large particles and, on average, have a larger resistance to void nucleation. These size effects generally apply to second populations of voids, if any, which most often involve submicron sizes [47,48], size X_5 in Fig. 3.

Another length that can play a major role in the failure process is the size of the plastic localization band X_1 which might appear as a result of damage induced softening. The localization band size directly scales with the void spacing $X_1 \approx X_0$, see Fig. 3. Mathematically, a plastic localization of this kind is a bifurcation resulting from the loss of ellipticity of the governing equations. The general formalism to address plastic localization has been discussed by Rice [93]. The specific problem of damage driven localization has been studied by many authors [78,94–96]. The generation of plastic localization bands depends not only on the void volume fraction but also on the loading conditions and on the geometry of the structure. This localization mechanism must not be confused with the void coalescence mechanism which depends on the void geometry and local stress state within the ligament between the voids. This confusion is easily made because the localization band thickness X_1 is not much different than the thickness of the localization zone X_2 associated with void coalescence which scales with the void radius [51,63]. Indeed, at coalescence, the ligament size is always on the order of the void radius [97]. Depending on the problem, plastic localization will or not develop before void coalescence. Ultimately, void coalescence will almost always take place. The ductility will be affected by the occurrence of plastic localization before coalescence. The general problem of ductility set by plastic localization (connected or not to the presence of damage) is outside the scope of this paper, though essential in some forming operations like deep drawing and in the analysis of the forming limit diagrams.

Now, the existence of these two lengths $X_1 \approx X_0$ and X_2 brings serious difficulties when modelling ductile failure. Indeed, before any localization, the problem is length independent, but as soon as localization sets in, the problem becomes

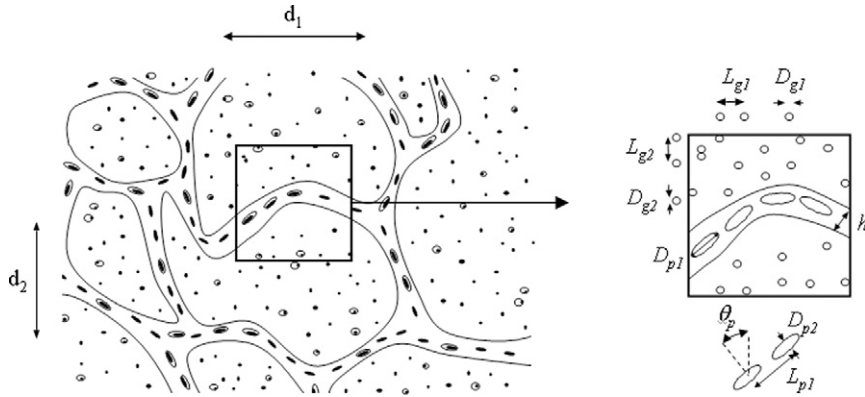


Fig. 4. Description of (a) the microstructure and failure mechanisms, and of (b) the idealized microstructure.
Fig. 4. Description (a) de la microstructure et des mécanismes de rupture, et (b) de la microstructure idéalisée.

inherently size dependent. The constitutive model described in Section 3.1 does not involve any length scale. Different solutions have been formulated in the literature to solve this problem. To our knowledge, no solution for embedding the two lengths $X_1 \approx X_0$ and X_2 has already been worked out. Let us briefly mention the solutions for introducing one length. The simplest solution in the context of FE simulations is to fix the element size as equal to the internal length X_1 or X_2 , e.g. [14]. This pragmatic solution has the drawback to mix the numerical solution procedure to the constitutive material description. Advanced solutions involve the development of non-local formulations, an area of continuous interest in ductile failure for almost 20 years [18,98–102]. Recently, Huespe et al. [103] have proposed a hybrid model. The material response is initially described by a Gurson model. When the loss of ellipticity is met, a weak discontinuity is embedded with a specific thickness and described by a traction separation law. The traction separation law depends on the stress triaxiality in order to keep the connection to the physics of the void growth mechanism.

As explained in Section 2, the importance of accounting for the lengths X_1 and/or X_2 is even more crucial when addressing the ductile tearing resistance, as the fracture toughness is directly proportional to the internal length. The problem of selecting the correct length X_1 and/or X_2 to set the fracture process zone height is still a matter of open debate. The methods mentioned in the previous paragraph permit the introduction of the length scale for modelling crack growth. Note that there is one class of problem where the lengths X_1 and/or X_2 do not have to be explicitly accounted for, i.e. when looking at crack growth within an infinite medium. This class of problem belongs to the so-called small scale yielding (SSY) formulation. In that case, the predicted energy release rate is directly applied and can be normalized by the internal length. It is an interesting approach for analyzing, from an academic viewpoint, the effect of microstructure on ductile tearing, while avoiding issues related to finite specimen sizes; see, for instance, one example in Section 4 or in [58,104].

In real metallic materials, especially the most complex ones involving several phases, and/or microstructure gradients, additional lengths and size effects can play a role and affect ductile failure. The presence for instance of softer or harder zones [21,105], of elongated bands of particles, of clustering effects [40,43], of weak zones in welds (see Section 5), or of precipitate free zones (see next section) can lead to significant change of ductility and or fracture toughness, and to anisotropy or rate effects. These additional microstructure based lengths must be taken into account in the model when building the multilevel scheme, most often through building FE models with realistic microstructure representations. The possibilities are infinite, and we will limit ourselves to two applications which illustrate how the methodology can be applied and the level of sophistication that can be attained nowadays with such kind of approaches.

4. Competition between inter- and transgranular failure in Al alloys

4.1. Description of the material and damage mechanisms

A typical example of multilevel ductile failure problem is the following. Many Al, Ti, Ni or Fe-based metallic alloys involve micron or submicron thick layers surrounding Grain Boundaries (GB) with a microstructure different from the bulk of the grain, e.g. [106–108]. In several circumstances, the GB layers are softer than the grain interior, due to a lack of nanoscale hardening precipitates. The presence of these soft zones favors a low toughness intergranular fracture mode. A classical example is given by the Al alloys of the 7xxx series with important implications in aeronautical applications. Ductile damage occurs both inside the grains and within the GB layers through the nucleation of voids by cracking or decohesion of large second phases, void growth and coalescence, see Fig. 4. The goal of the study [81] was to investigate the influence of the parameters describing the microstructure and of the flow properties on the cracking resistance and preferential crack path by treating the problem with different levels of details in the description of the microstructure. It is important to improve the understanding of the competition between intergranular and transgranular failure in order to support the optimization of the microstructure.

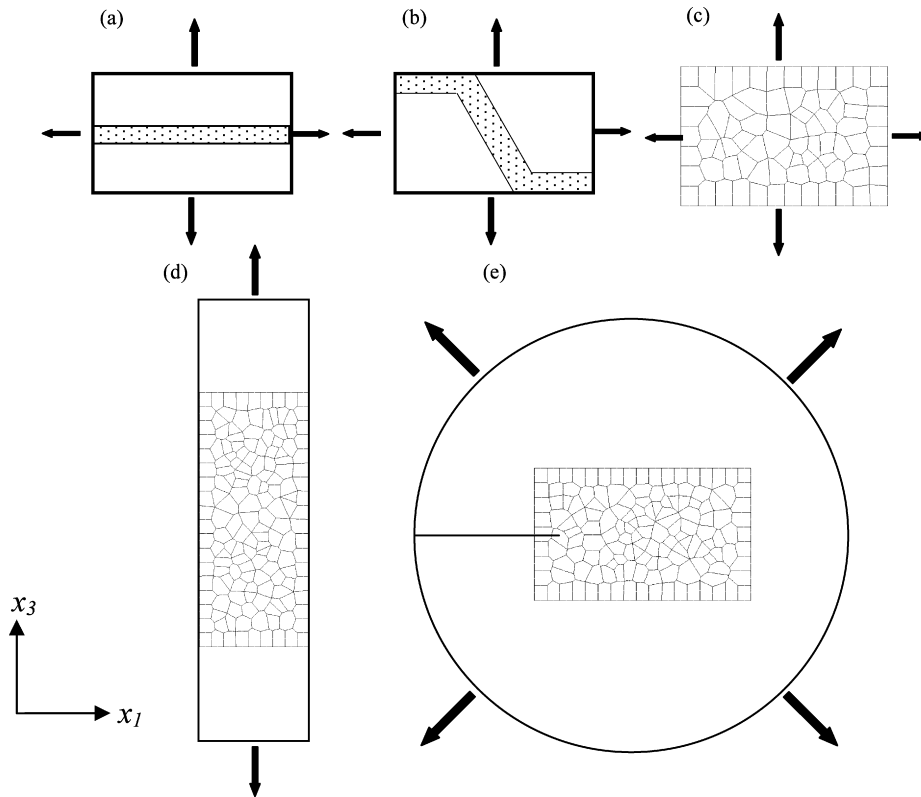


Fig. 5. Five models to simulate the damage evolution and cracking resistance of polycrystalline alloys involving soft grain boundary layers and hard grain interiors, see description in the text.

Fig. 5. Cinq modèles destinés à simuler l'évolution de l'endommagement et la résistance à la fissuration d'alliages polycristallins impliquant des zones molles le long des joints de grain et des intérieurs de grain durs, voir description détaillée dans le texte.

Whatever the description chosen for the microstructure, at least three phenomenological length scales are involved. At the lowest scale, a constitutive model relying on the Gologanu model for the void growth part, see Eqs. (4)–(9), the Thomason model for the void coalescence condition, see Eq. (16), and the coalescence model explained at the end of Section 3.2 [51] has been used to represent the response of an elastoplastic porous material region located either in the PFZ or in the grain interior. The voids are considered to be present from the beginning of the loading. Furthermore, the Al alloys under interest have a volume fraction of second phases smaller than a few percents and the loss of strengthening resulting from the particle fracture or decohesion can be safely neglected. Hence, the integrated homogenization-damage model described in Section 3.1 was not needed. No second population was taken into account. Nevertheless, in order to allow a realistic treatment of void growth and coalescence under various loading conditions, involving significant shear strains along the inclined grain boundaries, a specific effort was devoted to formulate void rotation laws based on the work of Kaisalam and Ponte-Castañeda's [82] and to use the generalized version of the coalescence condition for a localization at any possible orientation with respect to the main loading direction explained in Section 3.2, see also [81]. The second scale is the scale of a sub-material region involving a bilayer made of soft and hard regions. The third scale is the scale of the aggregate of grains, sometimes embedded in a homogenized medium making the transition to a fourth larger scale typical of a macroscopic structure or components. These three levels of description are treated using the FE method, as described next.

4.2. Description of the models and numerical procedures

The fracture mechanisms are investigated at different scales and with various levels of sophistication, using different representations of the microstructure and employing the FE method. The different models are shown in Fig. 5:

Model 1 – Bilayer model – Fig. 5(a). This model describes the response at the grain level by a soft zone sandwiched between two hard grains, essentially assuming that the competition in the damage and fracture evolution is controlled by the GB layers perpendicular to the main loading direction. This simple representation of the microstructure has been addressed in details in a former study [25].

Model 2 – Single grain model – Fig. 5(b). This model improves Model 1 by a more realistic description of the grain involving a hexagonal shape (which can be equiaxed or not) and GB layers inclined with respect to the main loading

Table 1

Values of the material parameters of the constitutive model, typical for Al alloys: σ_0/E is the ratio of yield stress to Young's modulus, ν is the Poisson ratio, n is the strain hardening exponent, f_0 is the initial void volume fraction, W_0 is the initial void shape, and λ_0 is the initial void distribution parameter.

Grain interior	σ_{0g}/E_g 10^{-3}	ν_g 0.35	n_g 0.05	f_{0g} 5×10^{-3}	W_{0g} 1	λ_{0g} 1
GB layer	σ_{0p}/E_p 2 to 10	ν_p 0.35	n_p 0.3	f_{0p} 5×10^{-2} to 6×10^{-3}	W_{0p} 1/3	λ_{0p} 1

direction. Periodic boundary conditions are enforced. Owing to the symmetries, the unit cell consists of only a portion of the grain.

Model 3 – Multigrain model under homogeneous loading conditions – Fig. 5(c). Compared to Model 2, the multi-grain representation provides statistical results, by dealing with more realistic grain shape and size distributions, and allows the coexistence of both failure modes and the simulation of complex crack paths.

Model 4 – Multigrain tensile test sample – Fig. 5(d). The multi-grain window is embedded into a tensile test sample, in order to simulate a test involving necking, therefore generating realistic information about ductility, fracture surface orientation, and crack path that can be compared to experimental results.

Model 5 – Small scale yielding (SSY) multigrain model – Fig. 5(e). The multigrain window is embedded into a large domain subjected to a K-field with a pre-existing macro-crack. The domain is large enough to enforce small scale yielding conditions and to generate geometry-independent J_R curves.

For each of these models, the GB layers (shown in Figs. 5 (a) and (b), but not in (c), (d) and (e)) are meshed with one or two elements over the thickness. The grain interiors are finely meshed, especially in Models 1 and 2. The multigrain box is constructed based on a Voronoi tessellation procedure. The models are all 2D plane strain. The response of the grain interior and GB layer is described by the same constitutive model, briefly outlined in Section 4.1. The hardening law for the material in the grain interior and in the GB layer is given by a power law description:

$$\frac{\sigma}{\sigma_0} = \frac{E\varepsilon}{\sigma_0} \quad \text{when } \sigma < \sigma_0 \quad (17)$$

$$\frac{\sigma}{\sigma_0} = \left(1 + \frac{E\varepsilon^p}{\sigma_0}\right)^n \quad \text{when } \sigma \geq \sigma_0 \quad (18)$$

where E is the Young's modulus, σ_0 is the yield stress, and n is the strain-hardening exponent. The material parameters used in all calculations reported in the present paper are typical for 7xxx Al alloys [106], see Table 1 with definitions. A subscript “g” (resp. “p”) is used when referring to the grain interior (resp. for the GB layer). The relative thickness of the GB layer with respect to the grain size, R_0 , is equal to 0.0525, the grain shape $W_{\text{grain}} = 1$, and the grain orientation $\theta_{\text{grain}} = 0^\circ$. The model has been implemented in an in-house FE code within a finite strain setting, as explained in details in [81].

4.3. Selected results and discussion

4.3.1. Single grain model (Model 2)

Fig. 6 shows stress-strain curves predicted with Model 2 for different yield stress ratios, using the parameters of Table 1. The transition from an intergranular fracture mode when the grain is much harder than the GB layer to transgranular fracture when the hardness mismatch gets smaller is clearly captured. Note that the predictions of the bilayer model (Model 1) [25] agree qualitatively well with the single grain model (Model 2). Quantitatively, the presence of inclined GBs tends to relax the constraint in the soft layers, favoring slightly more the transgranular failure mode.

4.3.2. Multigrain model under homogeneous loading conditions (Model 3)

Fig. 7 shows the variation for three different grain distributions of the fracture strain as a function of yield stress mismatch for different applied stress ratios Σ_{11}/Σ_{22} . Two distributions correspond to two different Voronoi tessellations (see Fig. 8 where the multigrain is embedded in a tensile sample) and one distribution is a perfect arrangement of identical hexagonal grains (equivalent to the single grain model). The results found with the two statistical distributions are almost identical (i.e. the number of grains is sufficient so that statistical differences are averaged out), and the ductility is significantly smaller than for the perfect hexagonal arrangement, especially in the intergranular regime. The Voronoi tessellation leads to weak crack paths, which are absent in the hexagonal distribution.

4.3.3. Uniaxial tension with necking

At the left hand side of Fig. 8, a zoom is shown to the necking region of samples loaded up to fracture, for the three different grain distributions depicted in Figs. 8 (a)–(c). Results are provided for both low yield stress mismatch (left column of snap-shots) leading to significant amount of necking before transgranular failure and large yield stress mismatch (right column of snap-shots) leading to small amounts of necking before intergranular failure. Again, a regular arrangement of grains provides an artificially high ductility. Transgranular failure shows evidence of cup and cone fracture combining flat

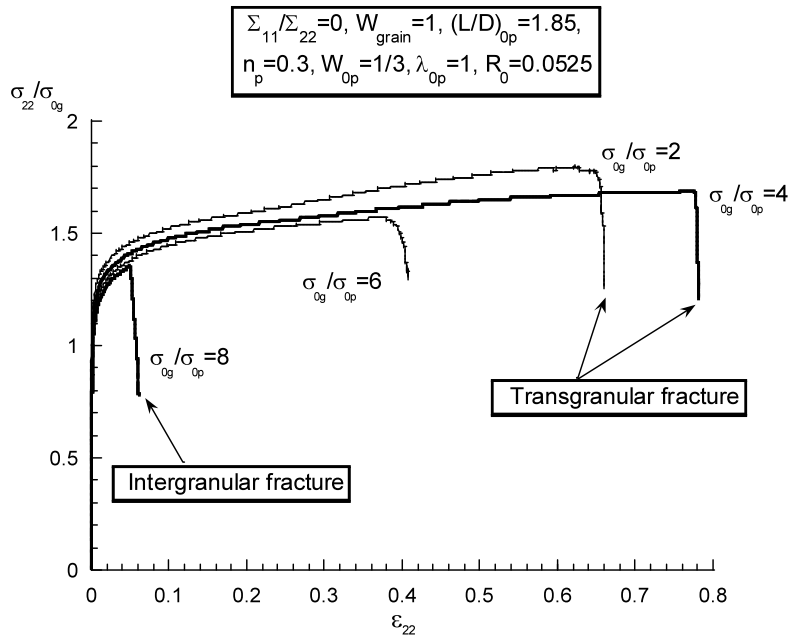


Fig. 6. Stress strain curves predicted with the single grain model (Model 2) for different ratios of yield stress between the grain interior and GB layer, under plane strain tension ($\Sigma_{11} = 0$). (The ratio $(L/D)_{op} = 1.85$ is similar to imposing $f_{op} = 5 \times 10^{-2}$.)

Fig. 6. Courbes contrainte déformation prédites par le modèle à un grain (modèle 2) pour différents rapports de limite d'élasticité entre l'intérieur du grain et les zones proches des joints de grain, en traction simple sous déformation plane ($\Sigma_{11} = 0$). (Le rapport $(L/D)_{op} = 1,85$ est similaire à imposer que $f_{op} = 5 \times 10^{-2}$.)

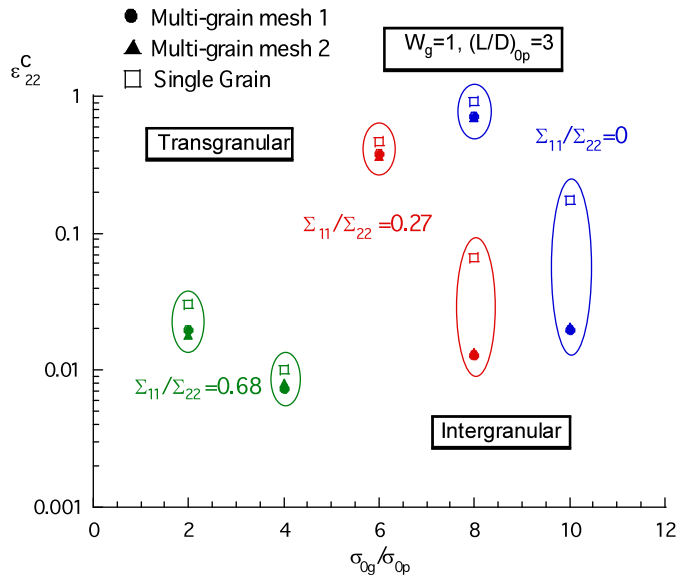


Fig. 7. Variation of the fracture strain as a function of the yield stress mismatch for different applied stress ratio and the three different grain arrangements shown in Fig. 8. (The ratio $(L/D)_{op} = 3$ is similar to imposing $f_{op} = 6 \times 10^{-3}$.)

Fig. 7. Variation de la déformation à rupture en fonction du rapport des limites d'élasticité pour différentes contraintes appliquées et trois différentes distributions de grains. (Le rapport $(L/D)_{op} = 3$ est similaire à imposer que $f_{op} = 6 \times 10^{-3}$.)

and shear type cracking (especially with regular grain distribution), while intergranular fracture leads to relatively flat fracture surfaces.

4.3.4. SSY multigrain model

Fig. 9 presents the J_R curves predicted with the SSY model for different yield stress mismatches. The effect of moving from intergranular to transgranular fracture is enormous in terms of tearing modulus. The crack profiles obtained for one

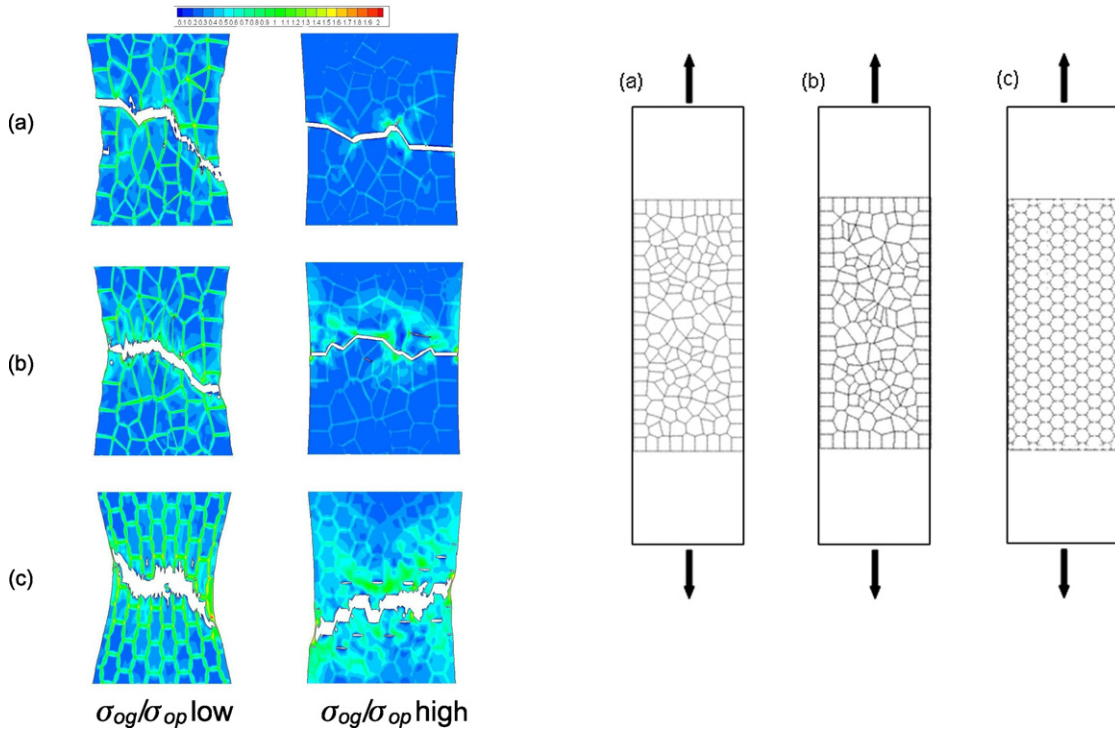


Fig. 8. Initial and final (fractured) configuration of tensile test samples for three different grain arrangements (a) to (c) shown on the right. The simulations are performed for a low (left column) and high (right column) yield stress mismatch leading to a transgranular large ductility failure and intergranular low ductility failure, respectively.

Fig. 8. Configuration initiale et finale des échantillons de traction pour les trois différentes distributions de grains de (a) à (c) montrées à la droite de la figure. Les simulations sont menées pour un faible (colonne de gauche) et un fort (colonne de droite) rapport des limites d'élasticité conduisant respectivement à une rupture intergranulaire très ductile et une rupture intergranulaire peu ductile.

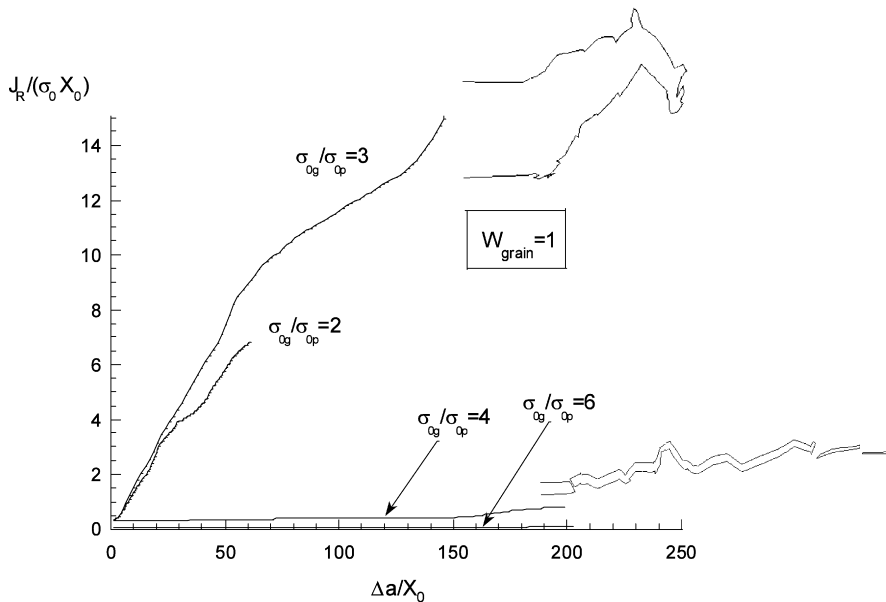


Fig. 9. Predictions obtained with SSY model in terms of J_R curves for different yield stress ratio and the crack profile for a low and high yield stress mismatch corresponding to transgranular and intergranular fracture modes, respectively.

Fig. 9. Prédiction obtenues avec le modèle de plasticité confinée (SSY) en terme de courbe de déchirure J_R pour différents rapports de limite d'élasticité, ainsi que les profils des fissures pour un faible et un fort rapport de limites d'élasticité correspondant respectivement aux modes de rupture transgranulaire et intergranulaire.

low and one high yield stress mismatch demonstrate that intergranular fracture involves, as expected, small amount of crack tip blunting and relatively straight crack path along the weak grain boundary layers.

The approach developed here having in mind the problem of the influence of PFZ on failure modes and ductility could be transposed to other problems involving competition between the failure in a soft or a hard zone, both involving a void growth damage mechanism. Of special interest are the cases of intrinsically heterogeneous materials [21,22,109] such as cast alloys with structural hardening (the core of the dendrite being equivalent to the grain interior, the eutectic particles equivalent to the grain boundary precipitates, and the intereutectic solid solution equivalent to the soft PFZ). In some situations, the soft zone may develop during the test such as the case of microstructure evolution in the vicinity of grain boundaries in diffusion controlled creep: in such situations, the present approach may be of some use to predict accelerated final void coalescence and creep failure. Another class of problems presenting heterogeneities at a larger scale is to be found in the joining technologies: brazed joint failure, heat affected zones in welding, and friction stirred joints as discussed in the next section.

5. Ductile failure in friction stir welded joints

Friction stir welding (FSW) is a novel welding process by which the parts to be welded do not reach the melting temperature (see reviews by Mishra and Ma [110], Nandan et al. [111] and Threadgrill et al. [112]). Due to the intense stirring and non-isothermal treatment of the material during welding, different evolutions of the microstructure and of the subsequent material properties are observed across the weldline. A FS-weld is typically divided into four regions: (1) the unaffected base material (BM); (2) the heat affected zone (HAZ); (3) the thermo-mechanically affected zone (TMAZ) exposed to high temperature with large heating and cooling rates as well as mechanical deformation; and (4) the nugget (NG) in the stir zone where recrystallization takes place.

A micromechanical damage model similar to the one presented in Section 3 (Eqs. (4)–(9)) and Eq. (16) has been applied to address ductile failure in friction stir welds made of aluminum alloy 6005A in the hardest T6 temper [113–117]. In the present paper, the focus will be on the behavior of a specific weld produced with an advancing speed of 1000 mm/min and a tool rotational speed of 1000 rpm. After welding, tensile specimens have been extracted from the weld in two perpendicular directions [115]: macro specimens (section 12.5 mm × 6 mm) involving the entire weld region with the loading direction perpendicular to the welding direction and mini tensile specimens (section 4 mm × 0.8 mm) probing the tensile properties in the various regions of the weld (i.e. in the BM, HAZ, TMAZ and NG) with the loading direction parallel to the welding direction. Fig. 10 presents the evolution of the tensile properties with respect to the distance from the weldline measured for the mini tensile specimens. The material is assumed to follow the extended Voce hardening law accounting for stage IV hardening [54,117]:

$$\sigma_y = \frac{\theta_0 - \theta_{IV}}{\beta} (1 - \exp(-\beta \varepsilon_p)) + \sigma_0 + \theta_{IV} \varepsilon_p \quad (19)$$

with $\beta = \beta_0 [1 - \frac{2\beta_0 \theta_{IV} \varepsilon_{p_ch}}{\theta_0}]^{-1}$ and ε_{p_ch} is the plastic strain for which $\sigma_y = (\theta_0/2\beta_0) + \sigma_0$.

Here, σ_y is the flow stress, ε_p is the plastic strain, σ_0 is the initial yield stress, θ_0 is the dislocation storage rate, β_0 is the dynamic recovery rate, and θ_{IV} is the stage IV hardening. Fig. 10 shows that the HAZ and NG are the weakest regions of the weld with a drop of yield strength of about half the initial yield strength of the base material. The HAZ is the weakest of all regions combining a low yield strength and a low strain hardening capacity (large β_0).

The FE model of the macro tensile test is shown in Fig. 11 involving the different zones of interest. The geometry of the zones has been determined by hardness maps on transverse sections and by macroscopic observations of the weld [115]. Each region of the model is described by the tensile properties extracted from the mini specimens. The material behavior is described either by the J_2 flow theory or by a fully coupled micromechanics damage model based on the Gologanu model, see Section 3.1. In the case of the J_2 flow theory, the calculations are run in two steps. The FE simulations provide the evolution of the overall strain components and stress triaxiality in the elements with the highest equivalent plastic strain. The history of the stress triaxiality as a function of the effective equivalent plastic strain is then applied to the damage model for the prediction of the onset of coalescence. This un-coupled two-steps approach for the multiscale problem brings the calculation time down to a few days on a personal computer compared to about one month on a powerful computer for the fully coupled damage model while not significantly affecting the predictions (see Table 2).

The parameters introduced in the damage model have been directly extracted from the characterization of the microstructures. Voids nucleate by the fracture of iron rich particles [54,19]. These particles have been analyzed by scanning electron microscopy giving a volume fraction f_p equal to 0.012 and an aspect ratio W_p equal to 0.6. Nucleation by particle fracture implies that the initial aspect ratio of the voids W_0 is very low (a value of 0.01 has been selected). The initial volume fraction of nucleated voids is calculated as $f_0 = (f_p W_0)/W_p$ [19,34,54]. The nucleation of flat voids due to the fracture of these iron-rich particles is stress-controlled [32]. A simple Beremin type void nucleation condition [69] is identified [54] based on a large variety of heat treatments on the 6005A aluminium alloy, avoiding the use of more complicated homogenization model like the one presented in Section 3.1. The void nucleation stress σ_c^{\min} is identified as equal to 400 MPa and the normal distribution of void nucleation is assumed to extend over $\Delta\sigma_c = 200$ MPa. This high value of the nucleation stress causes late void nucleation in low yield stress regions and early void nucleation on high yield stress regions, capturing

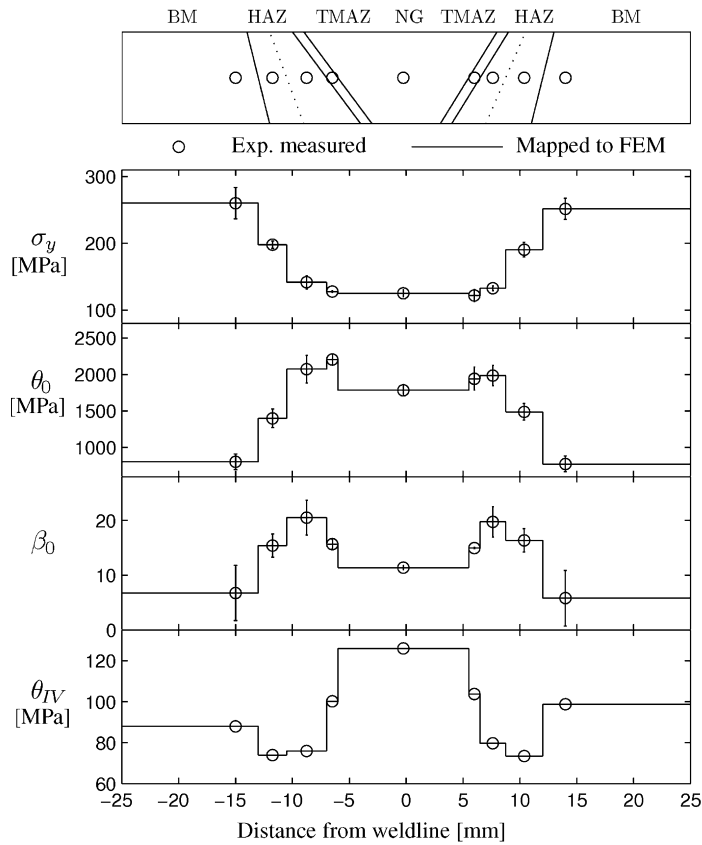


Fig. 10. Material properties on a transverse section of a FSW in AA6005A based on mini tensile specimens showing the initial yield stress σ_y , the dislocation storage rate θ_0 ; the dynamic recovery rate β_0 ; and the stage IV hardening θ_{IV} (estimated, see Ref. [117]). The top figure represents the distribution of the material properties on the FE mesh of the macro-specimens (from [117]).

Fig. 10. Propriétés matériaux dans une section du joint FSW en aluminium AA 6005A obtenues à partir de mini éprouvettes montrant la limite d'élasticité σ_y , le taux de stockage des dislocations θ_0 , le taux de restauration dynamique β_0 , et le taux d'écroutissage du stade IV θ_{IV} (pour l'estimation, voir Ref. [117]). La figure supérieure représente la façon dont les distributions des propriétés matériaux sont attribuées dans un maillage éléments finis des macro éprouvettes, voir [117].

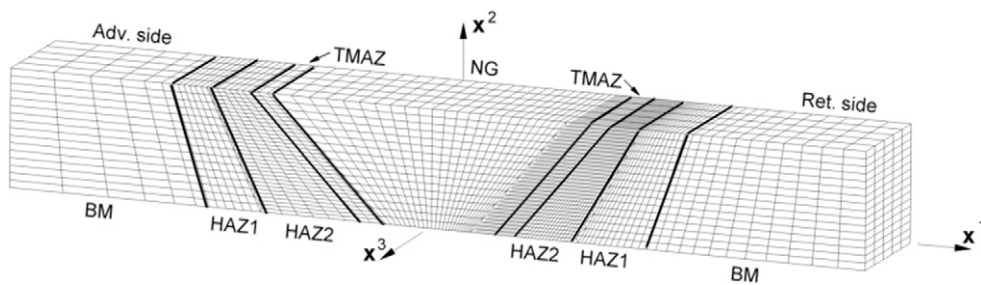


Fig. 11. Mesh used for the coupled 3D damage model of a macro-specimen containing the welded joints (from [117]).

Fig. 11. Maillage éléments finis utilisé pour les simulations 3D couplées avec endommagement des macro éprouvettes contenant un joint soudé, voir [117].

for instance the fracture strain evolution with heat treatment time of the 6005A alloy [54]. Note that industrial aluminum alloys generally contain dispersoids in addition to the typically μm size iron rich particles. These dispersoids are typically 50–100 nm in size and can intervene in the damage process as a second population of particles [48,118]. It has been shown by Simar et al. [54] that heat treated 6005A tensile specimens can show two populations of cavities if the material is in a hard state (typically in the T6 state). Now, the weld breaks in the HAZ which is a rather soft zone. No obvious second population has been observed on the fracture surfaces of the welds but it could still have a limited effect and hence slightly reduce the fracture strain compared to the ideal material assumed in the model.

Table 2 presents the results of the FE simulation of the macro-tensile test. The pseudo yield strength R_p , pseudo ultimate tensile strength R_u and pseudo engineering strain at necking e_u of the specimen involving the entire weld are well

Table 2

Measured and predicted transverse tensile properties of the weld (obtained by a macro tensile test). R_p is the pseudo yield strength, R_u is the pseudo ultimate tensile strength, e_u is the pseudo engineering strain at maximum load and ε_f is the fracture strain.

	R_p (MPa)	R_u (MPa)	e_u (%)	ε_f
Experiment	121	213	6.3	0.58
Coupled model [117]	123	216	7.9	0.68
J_2 – damage un-coupled model	125	212	7.6	0.68
J_2 – damage un-coupled model with 50% increased size of HAZ	124	208	7.5	0.703
J_2 – damage un-coupled model with a HAZ yield strength reduced by 20%	111	201	6.9	0.616

predicted. It has also been shown in Nielsen et al. [117] that the local strain distribution measured by digital image correlation during loading is well predicted. The damage model is able to accurately predict the fracture strain ε_f defined as $\varepsilon_f = \ln(A_0/A_f)$, where A_0 and A_f are the initial and final cross-section areas. The predictions of the fracture strain agree very well with the experimental values whether the damage model is coupled to the finite elements or not.

Table 2 shows also the effect of increasing the size of the weakest zone (the HAZ and the TMAZ) and the effect of decreasing the initial yield stress of the HAZ, which could arise as a result of post welding heat treatments or changing the welding conditions. If the width of the weak zone increases, the local stress triaxiality decreases since the size of the zone where plastic deformation localizes gets larger. The consequence is an increase of the fracture strain. Oppositely if the weak zone is even weaker, deformation localizes very early and the NG and TMAZ do not deform. This drastically increases the stress triaxiality causing earlier fracture, though slightly balanced by the low initial yield stress favoring later nucleation.

6. Conclusions

The applications discussed in the last two sections of the paper demonstrate the current level of maturity of the micromechanics based approach of ductile failure. Nevertheless, there is still much progress needed to incorporate in the models the different length scales listed in Section 3.3 using mathematically and physically sound formalism. The two main length scales are the void spacing and the void size which have well distinct effects, the first on the localization either by macroscopic bands or by the coalescence mechanism, the second on the void growth rate. Among others, the two length scales related to these two localization mechanisms are usually not distinguished in existing computational models. In addition to the length scales, the problem of properly treating the effect of the distribution of the position, size and shape of the voids is still an open issue. In the framework presented in this paper, it was tacitly assumed that the voids have the same size, shape and are arranged in a more or less periodic way (see e.g. [43] for an attempt at modelling realistic distribution effects). Finally, the interest of material scientists is not limited to linking microstructure to material properties but also to incorporate all the processing aspects in the picture. The friction stir welding problem addressed in the last section offers one possible example where the idea is to guide the development of better welds by playing with the process parameters and metallurgy. The objective is to couple the multiscale model for ductile failure to a chain of models involving a thermal evolution simulation during welding, precipitation kinetics, hardening and strain hardening [116] in order to control the entire history in a “materials by design” approach. This is indeed where the present type of approach will find the highest interest for physical metallurgy applications.

Acknowledgements

The long term interactions on the topic of ductile failure with J.-B. Leblond, Y. Bréchet, A.A. Benzerga and J.W. Hutchinson are gratefully acknowledged. F.S. acknowledges the support of the Walloon Region (DGTRE) and the Fonds Social Européen through a “FIRST EUROPE Objectif 3” project under the contract EPH3310300R0302/215284. C.T. acknowledges the support of Fond National de la Recherche Scientifique (FNRS) through a postdoctoral fellowship associated to the Hetmat project. A.S. is a postdoctoral researcher of the FNRS, Belgium. The calculations have been performed on the CISM-UCL, Belgium computer facilities. This research was carried out under the University Attraction Poles (IAP) Programme, financed by the Belgian Science Policy under contract P6/24.

References

- [1] A. Pineau, Review of fracture micromechanisms and a local approach to predicting crack resistance in low strength steels, in: D. François, et al. (Eds.), ICF 5, in: *Advances in Fracture Research*, vol. 2, Pergamon, 1981, pp. 553–577.
- [2] V. Tvergaard, Material failure by void growth to coalescence, *Adv. Appl. Mech.* 27 (1990) 83–151.
- [3] A. Pineau, T. Pardoen, Failure mechanisms of metals, in: *Comprehensive Structural Integrity Encyclopedia*, vol. 2, Elsevier, 2007, Chap. 6, on-line.
- [4] A.A. Benzerga, J.-B. Leblond, Ductile fracture by void growth to coalescence, *Adv. Appl. Mech.* (2010), in press.
- [5] C.F. Tipper, The fracture of metals, *Metallurgica* 39 (1949) 133–137.
- [6] K.E. Puttick, Ductile fracture in metals, *Philos. Mag.* 4 (1959) 964–969.

- [7] H.C. Rogers, Tensile fracture of ductile metals, *Trans. Metall. Soc. AIME* 218 (1960) 498–506.
- [8] C.D. Beachem, An electron fractographic study of the influence of plastic strain conditions upon ductile rupture processes in metals, *Trans. ASM* 56 (1963) 318.
- [9] J. Gurland, J. Plateau, The mechanism of ductile rupture of metals containing inclusions, *Trans. ASM* 56 (1963) 442–454.
- [10] F.A. McClintock, A criterion for ductile fracture by the growth of holes, *J. Appl. Mech.* 35 (1968) 363–371.
- [11] J.R. Rice, D.M. Tracey, On the ductile enlargement of voids in triaxial stress, *J. Mech. Phys. Solids* 17 (1969) 201–217.
- [12] Y. D'Escatha, J.C. Devaux, Numerical study of initiation, stable crack growth and maximum load with a ductile fracture criterion based on the growth of holes, in: J.D. Landes, J.A. Begley, G.A. Clarke (Eds.), *Elastic Plastic Fracture*, in: ASTM STP, vol. 668, American Society for Testing and Materials, Philadelphia, 1979, pp. 229–248.
- [13] A. Needleman, V. Tvergaard, An analysis of ductile rupture modes at a crack tip, *J. Mech. Phys. Solids* 35 (1987) 151–183.
- [14] L. Xia, C.F. Shih, J. Hutchinson, A computational approach to ductile crack growth under large scale yielding conditions, *J. Mech. Phys. Solids* 43 (1995) 389–413.
- [15] W. Brocks, D. Klingbeil, G. Kunecke, D.-Z. Sun, Application of the Gurson model to ductile tearing resistance, in: M. Kirk, A. Bakker (Eds.), *The Constraint Effects in Fracture Theory and Applications*, vol. 2, in: ASTM STP, vol. 1244, American Society for Testing and Materials, Philadelphia, 1995, p. 232.
- [16] K.C. Koppenhoefer, R.H. Dodds, Ductile crack growth in pre-cracked CVN specimens: numerical studies, *Nuclear Eng. Design* 180 (1998) 221–241.
- [17] R.M. McMeeking, Finite deformation analysis of crack-tip opening in elastic-plastic materials and implication for fracture, *J. Mech. Phys. Solids* 25 (1977) 357–381.
- [18] M. Brunet, F. Morestin, H. Walter, Damage identification for anisotropic sheet-metals using a non-local damage model, *Int. J. Damage Mech.* 13 (2004) 35–57.
- [19] D. Lassance, D. Fabrègue, F. Delannay, T. Pardoën, Micromechanics of room and high temperature fracture in 6xxx Al alloys, *Prog. Mater. Sci.* 52 (2007) 62–129.
- [20] T. Pardoën, Numerical simulation of low stress triaxiality ductile fracture, *Comput. Struct.* 84 (2006) 1641–1650.
- [21] B. Chéhab, Y. Bréchet, M. Véron, P.J. Jacques, G. Parry, J.-C. Glez, J.-D. Mithieux, T. Pardoën, Micromechanics of the high temperature damage in a dual phase stainless steel, *Acta Mater.* 58 (2010) 626–637.
- [22] L. Devillers-Guerville, J. Besson, A. Pineau, Notch fracture toughness of a cast duplex stainless steel: modelling of experimental scatter and size effects, *Nuclear Eng. Design* 168 (1997) 211–225.
- [23] S. Bugat, J. Besson, A. Pineau, Micromechanical modeling of the behavior of duplex stainless steels, *Comput. Mater. Sci.* 16 (1999) 158–166.
- [24] F. Rivalin, J. Besson, M. Di Fant, A. Pineau, Ductile tearing of pipeline-steel wide plates: II. Modeling of in-plane crack propagation, *Eng. Fract. Mech.* 68 (2001) 347–364.
- [25] T. Pardoën, D. Dumont, A. Deschamps, Y. Bréchet, Grain boundary versus transgranular ductile failure, *J. Mech. Phys. Solids* 51 (2003) 637–665.
- [26] M. Gologanu, J.-B. Leblond, G. Perrin, J. Devaux, Recent extensions of Gurson's model for porous ductile metals, in: P. Suquet (Ed.), *Continuum Micromechanics*, in: CISM Lectures Series, Springer, New York, 1997, p. 61.
- [27] T. Pardoën, Y. Marchal, F. Delannay, Thickness dependence of cracking initiation criteria in thin aluminum plates, *J. Mech. Phys. Solids* 47 (1999) 2093–2123.
- [28] T. Pardoën, F. Hachez, B. Marchioni, H. Blyth, A.G. Atkins, Mode I fracture of sheet metal, *J. Mech. Phys. Solids* 52 (2004) 423–452.
- [29] G. Lacroix, T. Pardoën, P.J. Jacques, On the fracture toughness of TRIP-assisted multiphase steels, *Acta Mater.* 56 (2008) 3900–3913.
- [30] N. Clément, Phase transformations and mechanical properties of the Ti-5553 β -metastable titanium alloy, Ph.D. thesis, Université catholique de Louvain, 2009.
- [31] A.S. Argon, J. Im, R. Safoglu, Cavity formation from inclusions in ductile fracture, *Metall. Trans. A* 6 (1975) 825–837.
- [32] M.N. Shabrov, E. Sylven, S. Kim, D.H. Sherman, L. Chuzhoy, C.L. Briant, A. Needleman, Void nucleation by inclusion cracking, *Metall. Mater. Trans. A* 35 (2004) 1745–1755.
- [33] B. Budiansky, J.W. Hutchinson, S. Slutsky, Void growth and collapse in viscous solids, in: H.G. Hopkins, M.J. Sewell (Eds.), *Mechanics of Solids. The Rodney Hill 60th Anniversary Volume*, Pergamon Press, Oxford, 1982, p. 13.
- [34] G. Huber, Y. Brechet, T. Pardoën, Void growth and void nucleation controlled ductility in quasi eutectic cast aluminium alloys, *Acta Mater.* 53 (2005) 2739–2749.
- [35] D. Lassance, F. Scheyvaerts, T. Pardoën, Growth and coalescence of penny-shaped voids in metallic alloys, *Eng. Fract. Mech.* 73 (2006) 1009–1034.
- [36] K.C. Liao, J. Pan, S.C. Tang, Approximate yield criteria for anisotropic porous ductile sheet metals, *Mech. Mater.* 26 (1997) 213–226.
- [37] F. Bron, J. Besson, A. Pineau, Ductile rupture in thin sheets of two grades of 2024 aluminum alloy, *Mater. Sci. Eng. A* 380 (2004) 356–364.
- [38] A. A Benzerga, J. Besson, A. Pineau, Anisotropic ductile fracture – Part I: experiments, *Acta Mater.* 52 (2004) 4623–4638.
- [39] A.A. Benzerga, J. Besson, A. Pineau, Anisotropic ductile fracture – Part II: theory, *Acta Mater.* 52 (2004) 4639–4650.
- [40] A. Needleman, A.S. Kushner, An analysis of void distribution effects on plastic flow in porous solids, *Eur. J. Mech. A/Solids* 9 (1990) 193–206.
- [41] V. Tvergaard, Interaction of very small voids with larger voids, *Int. J. Solids Struct.* 35 (1998) 3989–4000.
- [42] P.F. Thomason, *Ductile Fracture of Metals*, Pergamon Press, Oxford, 1990.
- [43] M.J. Worswick, Z.T. Chen, A.K. Pilkey, D. Lloyd, S. Court, Damage characterization and damage percolation modeling in aluminum alloy sheet, *Acta Mater.* 49 (2001) 2791–2803.
- [44] C. Tekoğlu, T. Pardoën, A micromechanics based damage model for composite materials, *Int. J. Plast.* 26 (2010) 549–569.
- [45] T.B. Cox, J.R. Low, An investigation of the plastic fracture of AISI 4340 and 18 nickel-200 grade maraging steels, *Metall. Trans. A* 5 (1974) 1457–1470.
- [46] G. Perrin, J.B. Leblond, Accelerated void growth in porous ductile solids containing two populations of cavities, *Int. J. Plast.* 16 (2000) 91–120.
- [47] J. Faleskog, C.F. Shih, Micromechanics of coalescence – I. Synergistic effects of elasticity, plastic yielding and multi-size-scale voids, *J. Mech. Phys. Solids* 45 (1997) 21–45.
- [48] D. Fabrègue, T. Pardoën, A constitutive model for elastoplastic solids containing primary and secondary voids, *J. Mech. Phys. Solids* 56 (2008) 719–741. Corrigendum to “A constitutive model for elastoplastic solids containing primary and secondary voids” *J. Mech. Phys. Solids* 57 (2009) 869–870.
- [49] P.F. Thomason, Three-dimensional models for the plastic limit-load at incipient failure of the intervoid matrix in ductile porous solids, *Acta Metall.* 33 (1985) 1079–1085.
- [50] T. Pardoën, I. Doghri, F. Delannay, Experimental and numerical comparison of void growth models and void coalescence criteria for the prediction of ductile fracture in copper bars, *Acta Mater.* 46 (1998) 541–552.
- [51] F. Scheyvaerts, P.R. Onck, T. Pardoën, A new model for void coalescence by internal necking, *Int. J. Damage Mech.* 19 (2010) 95–126.
- [52] J.W. Hancock, A.C. Mackenzie, On the mechanisms of ductile failure in high-strength steels subjected to multi-axial stress-states, *J. Mech. Phys. Solids* 14 (1977) 147–169.
- [53] B. Marini, F. Mudry, A. Pineau, Experimental study of cavity growth in ductile rupture, *Eng. Fract. Mech.* 6 (1985) 989–996.
- [54] A. Simar, K.L. Nielsen, B. de Meester, V. Tvergaard, T. Pardoën, Micro-mechanical modelling of ductile failure in 6005A aluminium using a physics based strain hardening law including stage IV, *Eng. Fract. Mech.* 77 (2010) 2491–2503.
- [55] V. Tvergaard, J.W. Hutchinson, Two mechanisms of ductile fracture: void by void growth versus multiple void interaction, *Int. J. Solids Struct.* 39 (2002) 3581–3597.

- [56] A. Needleman, V. Tvergaard, An analysis of ductile rupture in notched bars, *J. Mech. Phys. Solids* 32 (1984) 461–490.
- [57] J. Besson, D. Steglich, W. Brocks, Modelling of plane strain ductile rupture, *Int. J. Plast.* 19 (2003) 1517–1541.
- [58] T. Pardoen, J.W. Hutchinson, Micromechanics-based model for trends in toughness of ductile metals, *Acta Mater.* 51 (2003) 133–148.
- [59] A. Gurson, Continuum theory of ductile rupture by void nucleation and growth: part I – Yield criteria and flow rules for porous ductile media, *J. Eng. Mater. Technol.* 99 (1977) 2–15.
- [60] M. Gologanu, J.B. Leblond, J. Devaux, Approximate models for ductile metals containing non-spherical voids – case of axisymmetric prolate ellipsoidal cavities, *J. Mech. Phys. Solids* 41 (1993) 1723–1754.
- [61] M. Gologanu, J.B. Leblond, J. Devaux, Approximate models for ductile metals containing non-spherical voids – case of axisymmetric oblate ellipsoidal cavities, *J. Eng. Mater. Technol.* 116 (1994) 290–297.
- [62] V. Monchiet, O. Cazacu, E. Charkaluk, D. Kondo, Macroscopic yield criteria for plastic anisotropic materials containing spheroidal voids, *Int. J. Plast.* 24 (2008) 1158–1189.
- [63] T. Pardoen, J.W. Hutchinson, An extended model for void growth and coalescence, *J. Mech. Phys. Solids* 48 (2000) 2467–2512.
- [64] O. Pierard, I. Doghri, A study of various estimates of the macroscopic tangent operator in the incremental homogenization of elasto-plastic composites, *Int. J. Multiscale Comput. Eng.* 4 (2006) 521–543.
- [65] I. Doghri, C. Friebl, Effective elasto-plastic properties of inclusion-reinforced composites study of shape, orientation and cyclic response, *Mech. Mater.* 37 (2005) 45–68.
- [66] I. Doghri, A. Ouair, Homogenization of two-phase elasto-plastic composite materials and structures – study of tangent operators, cyclic plasticity and numerical algorithms, *Int. J. Solids Struct.* 40 (2003) 1681–1712.
- [67] M. Bornert, T. Bretheau, P. Gilormini, Homogénéisation en mécanique des matériaux, 1. Matériaux aléatoires élastiques et milieux périodiques, HERMES Science, Paris, 2001.
- [68] C. Chu, A. Needleman, Void nucleation effects in biaxially stretched sheets, *J. Eng. Mater. Technol.* 102 (1980) 249–256.
- [69] F.M. Beremin, Cavity formation from inclusions in ductile fracture of A508 steel, *Metall. Trans. A* 12 (1981) 723–731.
- [70] J.B. Leblond, G. Perrin, J. Devaux, An improved Gurson-type model for hardenable ductile metals, *Eur. J. Mech. A/Solids* 14 (1995) 499–527.
- [71] H. Klöcker, V. Tvergaard, Growth and coalescence of non-spherical voids in metals deformed at elevated temperature, *Int. J. Mech. Sci.* 25 (2003) 1283–1308.
- [72] M. Grange, J. Besson, E. Andrieu, An anisotropic Gurson model to represent the ductile rupture of hydrided Zircaloy–4 sheets, *Int. J. Fract.* 105 (2000) 273–293.
- [73] A.A. Benzerga, J. Besson, R. Batisse, A. Pineau, Synergistic effects of plastic anisotropy and void coalescence on fracture mode in plane strain, *Mod. Simul. Mater. Sci. Eng.* 10 (2002) 73–102.
- [74] S.M. Keralavarma, A. Benzerga, An approximate yield criterion for anisotropic porous media, *C. R. Mécanique* 336 (2008) 685–692.
- [75] M. Mear, J.W. Hutchinson, Influence of yield surface curvature on flow localization in dilatant plasticity, *Mech. Mater.* 4 (1985) 395–407.
- [76] J. Besson, C. Guillemer-Neel, An extension of the Green and Gurson models to kinematic hardening, *Mech. Mater.* 35 (2003) 1–18.
- [77] U. Mühlich, W. Brocks, On the numerical integration of a class of pressure-dependent plasticity models including kinematic hardening, *Comput. Mech.* 31 (2003) 479–488.
- [78] K. Nahshon, J.W. Hutchinson, Modification of the Gurson Model for shear failure, *Eur. J. Mech. A/Solids* 27 (2008) 1–17.
- [79] P.F. Thomason, A theory for ductile fracture by internal necking of cavities, *J. Institute Metals* 96 (1968) 360–365.
- [80] P.F. Thomason, A three-dimensional model for ductile fracture by the growth and coalescence of microvoids, *Acta Metall.* 33 (1985) 1087–1095.
- [81] F. Scheyvaerts, P.R. Onck, T. Pardoen, Multiscale modelling of ductile fracture in heterogeneous metallic alloys, Ph.D. thesis, Université catholique de Louvain, 2009.
- [82] M. Kaisalam, P. Ponte-Castañeda, A general constitutive theory for linear and nonlinear particulate media with microstructure evolution, *J. Mech. Phys. Solids* 46 (1998) 427–465.
- [83] S.K. Yerra, C. Tekoğlu, F. Scheyvaerts, L. Delannay, A. Van Bael, P. Van Houtte, T. Pardoen, Void growth and coalescence in single crystals, *Int. J. Solids Struct.* 47 (2010) 1016–1029.
- [84] W. Brocks, D.Z. Sun, A. Hömig, Verification of the transferability of micromechanical parameters by cell model calculations with viscoplastic materials, *Int. J. Plast.* 11 (1995) 971–989.
- [85] X. Gao, J. Kim, Modelling of ductile fracture: significance of void coalescence, *Int. J. Solids Struct.* 43 (2006) 6277–6293.
- [86] J. Koplik, A. Needleman, Void growth and coalescence in porous plastic solids, *Int. J. Solids Struct.* 24 (1988) 835–853.
- [87] A.A. Benzerga, Micromechanics of coalescence in ductile fracture, *J. Mech. Phys. Solids* 50 (2002) 1331–1362.
- [88] V. Tvergaard, Studies of void growth in a thin ductile layer between ceramics, *Comput. Mech.* 20 (1997) 186–191.
- [89] J.B. Leblond, G. Mottet, A theoretical approach of strain localization within thin planar bands in porous ductile materials, *C. R. Mécanique* 336 (2008) 176–189.
- [90] N.A. Fleck, J.W. Hutchinson, Strain gradient plasticity, *Adv. Appl. Mech.* 33 (1997) 295–361.
- [91] J. Wen, Y. Huang, K.C. Hwang, C. Liu, M. Li, The modified Gurson model accounting for the void size effect, *Int. J. Plast.* 21 (2005) 381–395.
- [92] C.F. Niordson, Strain gradient plasticity effects in whisker-reinforced metals, *J. Mech. Phys. Solids* 51 (2003) 1863–1883.
- [93] J.R. Rice, The localization of plastic deformation, in: W.T. Koiter (Ed.), *Theoretical and Applied Mechanics*, North-Holland Publ. Co., 1976, pp. 207–220.
- [94] A. Needleman, J.R. Rice, Limits to ductility set by plastic flow localization, in: D.P. Koistinen, N.M. Wang (Eds.), *Mechanics of Sheet Metal Forming*, Plenum Press, New York, 1978, p. 237.
- [95] A. Needleman, V. Tvergaard, Analyses of plastic flow localization in metals, *Appl. Mech. Rev.* 45 (1992) S3–S18.
- [96] H. Yamamoto, Conditions for shear localization in the ductile fracture of void-containing materials, *Int. J. Fract.* 14 (1978) 347–365.
- [97] L.M. Brown, J.D. Embury, The initiation and growth of voids at second phase particles, in: *Proc. Third Int. Conf. on the Strength of Metals and Alloys, ICMA 3*, Cambridge, England, 1973, p. 164.
- [98] J.-B. Leblond, G. Perrin, J. Devaux, Bifurcation effects in ductile metals with nonlocal damage, *J. Appl. Mech.* 61 (1994) 236–242.
- [99] V. Tvergaard, A. Needleman, Effects of non local damage in porous plastic solids, *Int. J. Solids Struct.* 32 (1995) 1063–1077.
- [100] F. Reusch, B. Svendsen, D. Klingbeil, Local and non-local Gurson-based ductile damage and failure modelling at large deformation, *Eur. J. Mech. A/ Solids* 22 (2003) 770–792.
- [101] M.G.D. Geers, Finite strain logarithmic hyperelasto-plasticity with softening: a strongly nonlocal implicit gradient framework, *Comput. Methods Appl. Mech. Eng.* 193 (2004) 3377–3401.
- [102] J. Mediavilla, R.H.J. Peerlings, M.G.D. Geers, A nonlocal triaxiality-dependent ductile damage model for finite strain plasticity, *Comput. Methods Appl. Mech. Eng.* 66 (2006) 661–688.
- [103] A.E. Huespe, A. Needleman, J. Oliver, P.J. Sánchez, A finite thickness band method for ductile fracture analysis, *Int. J. Plast.* 25 (2009) 2349–2365.
- [104] V. Tvergaard, J.W. Hutchinson, The relationship between crack growth resistance and fracture process parameters in elastic plastic solids, *J. Mech. Phys. Solids* 40 (1992) 1377–1397.
- [105] D. Steglich, W. Brocks, J. Heerens, T. Pardoen, Anisotropic ductile damage modelling of Al2024 alloys, *Eng. Fract. Mech.* 75 (2008) 3692–3706.
- [106] D. Dumont, A. Deschamps, Y. Bréchet, A model for predicting fracture mode and toughness in 7000 series aluminium alloys, *Acta Mater.* 52 (2004) 2529–2540.

- [107] T.F. Morgeneyer, M.J. Starink, S.C. Wang, I. Sinclair, Quench sensitivity of toughness in an Al alloy: direct observation and analysis of failure initiation at the precipitate-free zone, *Acta Mater.* 56 (2008) 2872–2884.
- [108] T. Krol, D. Baither, E. Nembach, The formation of precipitate free zones along grain boundaries in a superalloy and the ensuing effects on its plastic deformation, *Acta Mater.* 52 (2004) 2095–2108.
- [109] T. Pardoën, Y. Bréchet, Influence of microstructure driven strain localisation on ductile fracture of metallic alloys, *Philos. Mag.* 84 (3–5) (2004) 269–298.
- [110] R.S. Mishra, Z.Y. Ma, Friction stir welding and processing, *Mater. Sci. Eng. R* 50 (2005) 1–78.
- [111] R. Nandan, T. DebRoy, H.K.D.H. Bhadeshia, Recent advances in friction-stir welding – process, weldment structure and properties, *Prog. Mater. Sci.* 53 (2008) 980–1023.
- [112] P.L. Threadgill, A.J. Leonard, H.R. Shercliff, P.J. Withers, Friction stir welding of aluminium alloys, *Int. Mater. Rev.* 54 (2009) 49–93.
- [113] A. Simar, J. Lecomte-Beckers, T. Pardoën, B. de Meester, Effect of boundary conditions and heat source distribution on temperature distribution in friction stir welding, *Sci. Technol. Weld. Joining* 11 (2006) 170–176.
- [114] A. Simar, T. Pardoën, B. de Meester, Effect of rotational material flow on temperature distribution in friction stir welds, *Sci. Technol. Weld. Joining* 12 (4) (2007) 324–332.
- [115] A. Simar, Y. Bréchet, B. de Meester, A. Denquin, T. Pardoën, Microstructure, local and global mechanical properties of friction stir welds in aluminium alloy 6005A-T6, *Mater. Sci. Eng. A* 486 (2008) 85–95.
- [116] A. Simar, Y. Bréchet, B. de Meester, A. Denquin, T. Pardoën, Sequential modelling of local precipitation, strength and strain hardening in friction stir welds of an aluminium alloy 6005A-T6, *Acta Mater.* 55 (2007) 6133–6143.
- [117] K.L. Nielsen, T. Pardoën, V. Tvergaard, B. de Meester, A. Simar, Modelling of plastic flow localisation and damage development in friction stir welded 6005A aluminium alloy using physics based strain hardening law, *Int. J. Solids Struct.* 47 (2010) 2359–2370.
- [118] C. Gallais, A. Simar, D. Fabrègue, A. Denquin, G. Lapasset, B. de Meester, Y. Bréchet, T. Pardoën, Multiscale analysis of the strength and ductility of 6056 aluminium friction stir welds, *Metall. Mater. Trans. A* 38 (2007) 964–981.